Superbeam single horn thermo-mechanical and multiphysics study and integration of 4-horns

Report on the Cracow team contribution to EuroNu project in 2010-2011

J. Bielski, P. Cupiał, M. S. Kozień, Ł. Łacny,
B. Skoczeń, B. Szybiński, A. Ustrzycka, A. Wróblewski

Cracow, January 2012

Contents

Foreword

The present report covers the activities of Cracow team during the period 2010-2011. The report addresses thermo-mechanical and multi-physics studies with respect to single horn as well as the integration issues related to 4-horns assembly. The thermo-mechanical quasi-static analysis contains estimation of temperature and primary as well as secondary stress distributions in the horn wall. Here, a coupled thermo-mechanical problem has been solved, given the combined loads resulting from current pulses and particle flux. A single spray cooling system has been taken into account. Complementary to the quasi-static analysis, a dynamic study of horn subjected to excitations generated by different sources has been carried out. In this part of report the dynamic stresses due to transient Joule heating, secondary particles and magnetic pulses have been estimated. A coupled magneto-solid approach has been applied. One of the fundamental problems to be solved is the fatigue life estimation related to cyclic loads acting on the horn. Here, the spectral method in frequency domain based on FFT and PSD analyses has been implemented. Some hints on corrosion fatigue and influence of welding are also included. Another important problem consists on estimation of degradation of material properties due to irradiation. The most sensitive part of the horn, located in direct proximity of the target has been analysed. The lifetime prediction in terms of number of beam cycles as a function of maximum dpa on cycle has been presented. The integration studies comprise the design of the support system for 4-horns assembly. Here, a cantilever support for single horn as well as various supporting frame concepts were developed. This part of the report is evolving as a follow up of the general 4-horns integration scheme, including radiation shelters and transport issues. Another part of integration studies is focused on the target-horn assembly scheme and effect of target on the cylindrical part of the horn. It is worth pointing out, that in the course of work on the present report some discrepancies in terms of geometrical data were detected. In most of the

cases they remain without major influence on the presented results. Finally, this report should be regarded as a draft version and will be upgraded in the course of further work carried out by the end of the project.

Chapter 1

Thermo-mechanical analysis of the horn

1.1 Temperature level and thermal stress level in the horn.

A sketch of simplified geometry of the axial cross section of the horn structure considered is shown in figure 1.1 and the dimensions are given in Tab 1.1. The horn structure is analyzed as axially-symmetric one with the axis z of rotational symmetry. The data were reported in May, 2011 by P. Cupiał and A. Wróblewski.

Table 1.1: Dimensions of the horn (in [mm])

L_1	589	$r_1 = r_2$	108
L_2	469	R_1	30
L_3	603	R_2	191
L_4	475	R_3	359
L_5	10.8	$t_1 = t_2 = t_3 = t_4$	3
L^{tg}	780	R^{tg}	6

In order to meet physics requirements it is assumed that the horn structure will be made of aluminum alloy. (e.g. Aluminum, 6082, T6)

The numerical analysis of the horn - distribution of horn temperature as well as stresses was performed with the ANSYS finite element code.

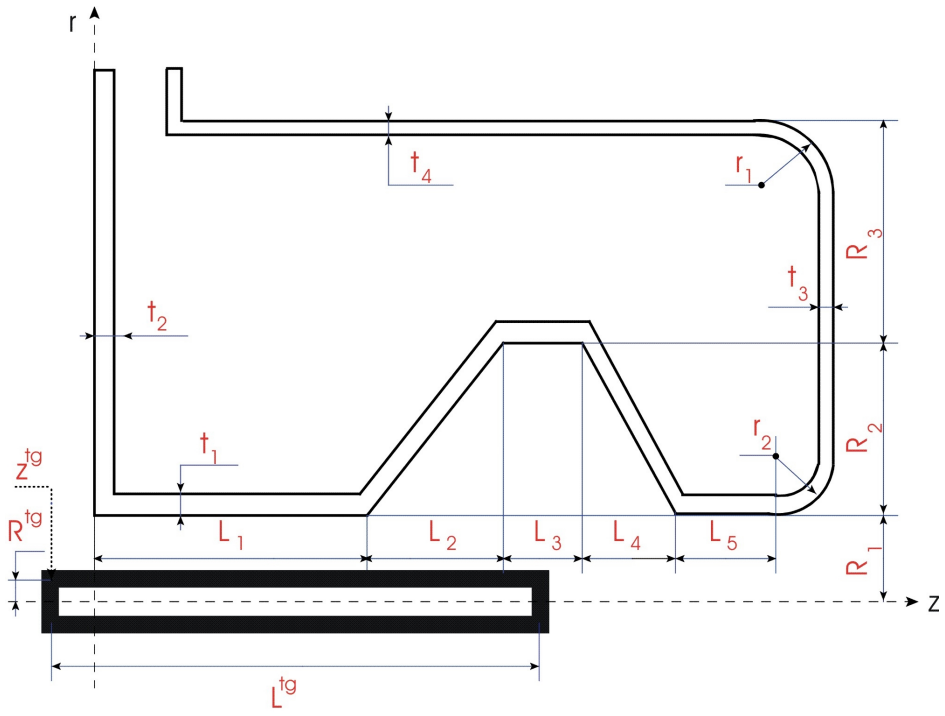

Figure 1.1: Simplified axial cross section of horn geometry

1.1.1 Thermal loads

The described structure is subjected to various types of heat loadings resulting from current pulses, magnetic field, kinetic energy of proton beam. The main constraint, which limits the structure endurance is attributed to the maximum allowable stress or to the maximum temperature during service. In case of aluminum alloys the maximum service temperature is estimated for 110° (∼380 K). Above this temperature the rapid decrease of mechanical properties like yield and ultimate stress is observed. High current pulses and energy of particles are the main sources of large heat energy generated in the horn shell, which result in temperature increase. Fig. 1.2 shows the deposition of heat power along the axi-symmetric cross section of the horn resulting from current pulses (300 or 350 kA) and secondary particle energy. As can be seen, the whole circumference of the cross section is divided into several segments, in which various values of cooling intensity are admitted and investigated. The

presented power values serve as the heat sources power in thermal calculations. The most severe conditions appear on the inside part of horn in the vicinity of the target beam (on the waist). Depending on the applied design solution this area is the crucial zone from the point of view of temperature increase.

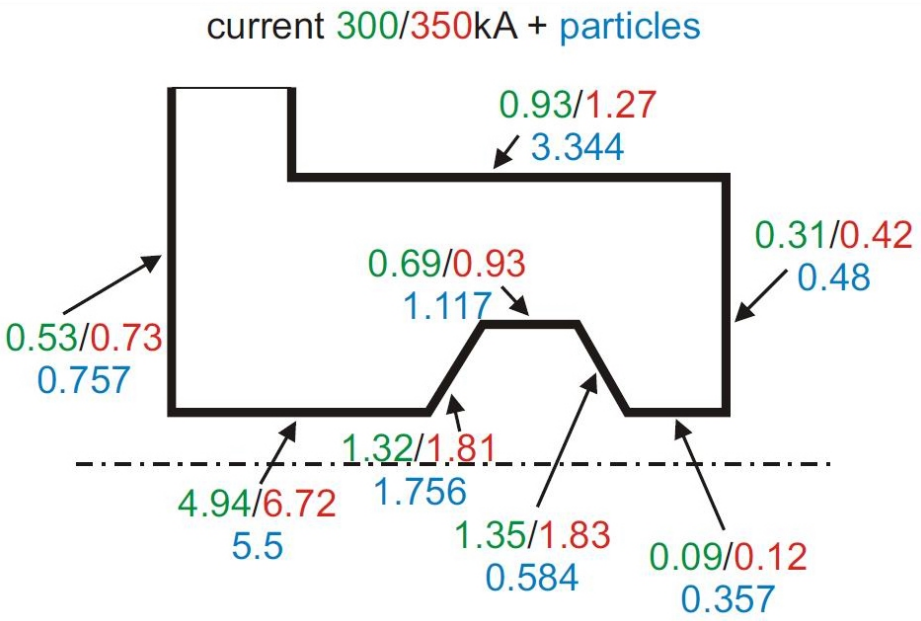

Figure 1.2: Distribution of heat power [kW] resulting from current pulses and particle in the horn wall volume

1.1.2 Cooling system

It has been decided before that horn cooling will be achieved by means of water sprays. In order to verify the possibilities of various cooling scenarios numerical analysis of the horn with different heat transfer coefficients applied to various faces was presented in May, 2011. After discussion of feasibility, one cooling system of water sprays acting inside the horn is chosen and analysed now. It is assumed that no water or air flow outside the horn is admitted, so that the heat exchange outside the horn is regarded as simple heat conduction in dry air. Inside of the horn the water sprays are located in order to provide high cooling rate. This is an effective cooling system for which the convection coefficient is of the order of 1000 $W/m^2/K$. Additionally, the heat conduction

in dry air inside the horn is analysed as an option. Hence, two extremes are estimated, namely the one without the air inside horn and the other with dry air in it. Following the power deposition, the intensity of cooling is proposed with analogous division to sections presented in Fig. 1.3.

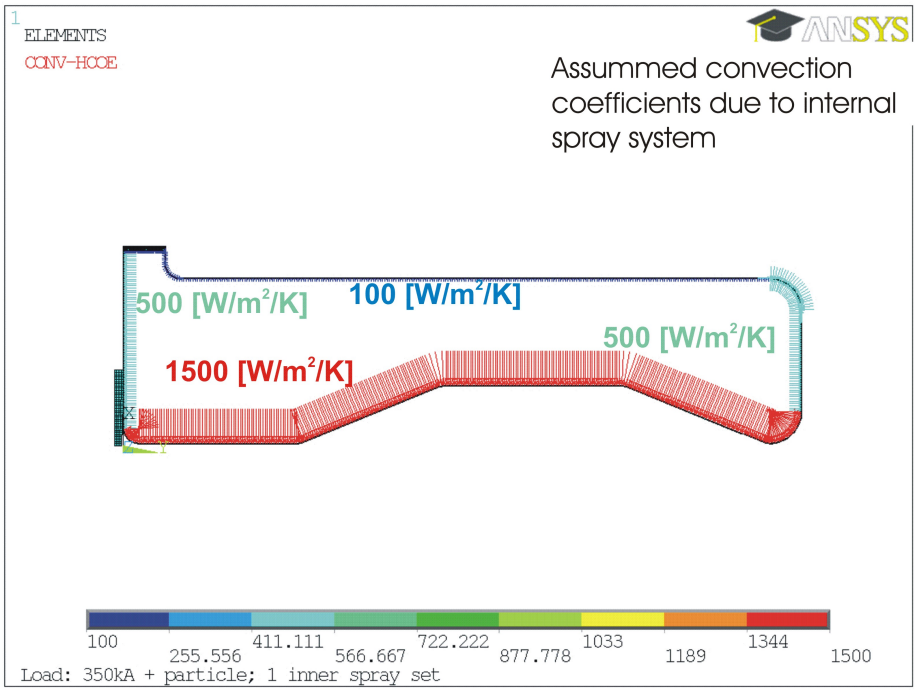

Figure 1.3: Assumed convection coefficients due to internal spray system

It is accepted that due to sufficiently increased water discharge, the convection coefficient reaches a level of 1500 W/m^2/K along the most heated surfaces. It is further assumed that water from sprays will wet the horn exit plates (the value of convection coefficient of 500 W/m^2/K) and the external skin (the value of convection coefficient of 100 W/m^2/K). For all the faces the bulk temperature is assumed of 293 K. The 500 K is taken for temperature of the external surface of the target.

Figure 1.4 and 1.5 present the temperature distribution for the value of current 350 kA and for the case with no heat convection in the air inside the horn. The maximum is $T_{max} = 338$ K. The distribution of the temperature in the air between the horn and the target is given in figure 1.7. The maximal equivalent (von Mises) stress induced by the temperature distribution in the

horn is estimated for 12.5 MPa and is met at the external circumference due to imposed support conditions which block the radial extension of the shell (fig. 1.7). Verifying calculations were performed for various convection coefficients on the wall closest to the target. Results are summarized in the table 1.2. One may observe that reduction of that coefficient down to 500 $W/m^2/K$ would result in unacceptable temperature level with still save stress level.

Table 1.2: Influence of the convection coefficient value

convection coefficient $W/m^2/K$	1500	1000	500
maximal temperature K	337.5	359.5	425.0
maximal equivalent stress MPa	12.5	12.5	15.6

The extreme values of temperature as well as of equivalent stress are even lower if the heat convection in the air inside the horn is admitted. Namely, the maximal temperature is estimated for 315 K (fig. 1.8), whereas the maximal equivalent stress is of 6.2 MPa and is observed at the high curvature region of the horn wall (fig. 1.9).

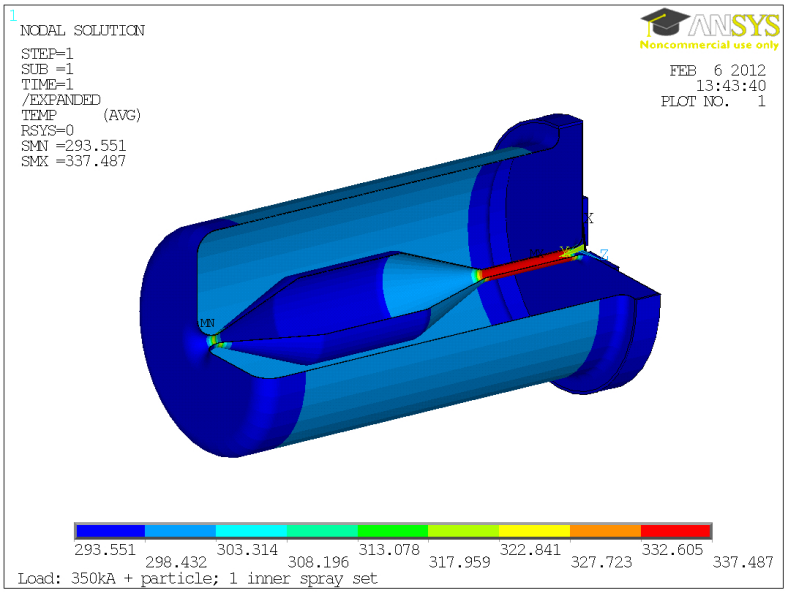

Figure 1.4: Temperature distribution in the horn (no convection in air inside)

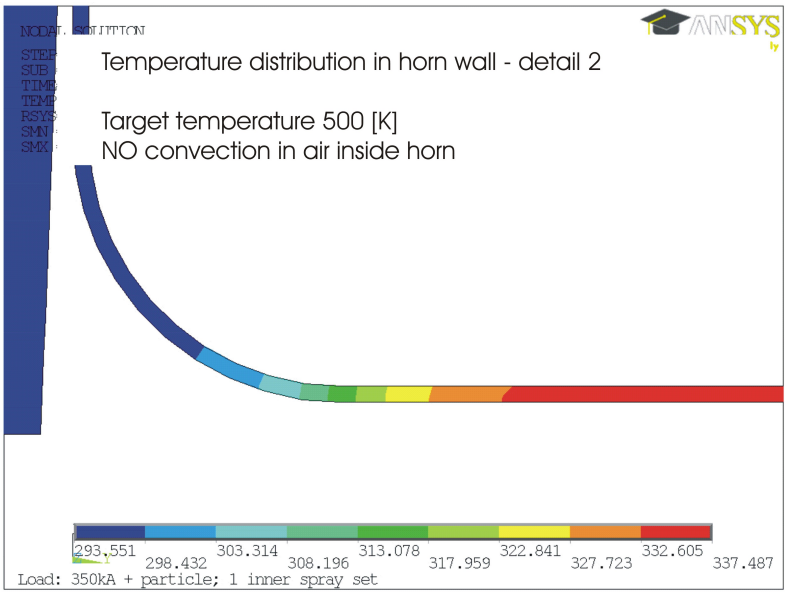

Figure 1.5: Temperature distribution in the horn (no convection in air inside) - detail

1.1.3 Conclusions and remarks

1. The temperature level in the horn wall is estimated save provided the water spray system is efficient enough i.e. the convection coefficient (film coefficient) is at least 1000 W/m^2/K.

2. The temperature is low enough regardless the heat conduction in the air inside the horn is admitted or not.

3. The stress level is estimated save for any case if the static stress is considered. The separate study discusses the influence of stresses on the material radiation damage.

4. The radiation heat exchange is not considered here. However, a simple test performed for two coaxial cylinders of dimensions following the target external diameter and the horn internal diameter as well as of temperatures of even 1500 K (for target) and 300 K for horn proved that this way of heat exchange is negligible for the case considered.

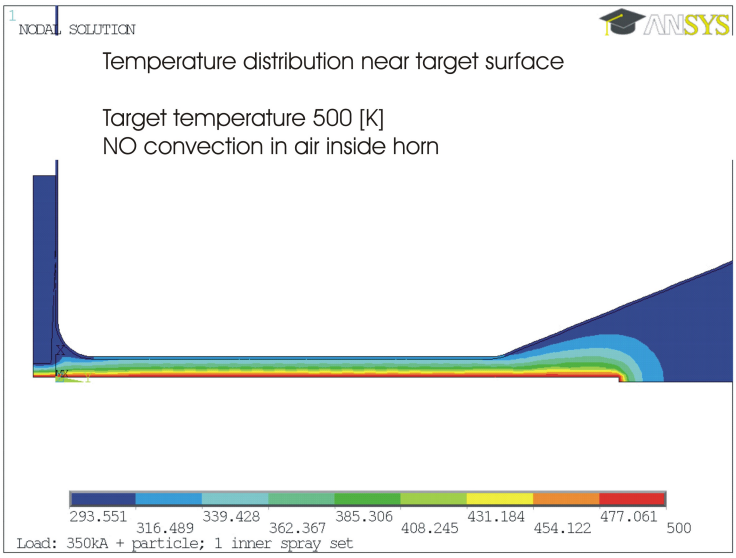

Figure 1.6: Temperature distribution in the air between the target and the horn (no convection in air inside)

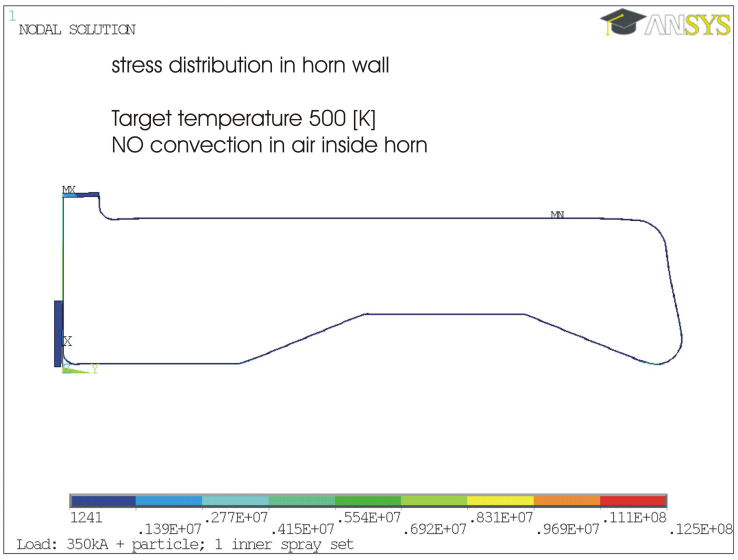

Figure 1.7: Equivalent stress distribution in the horn (no convection in air inside)

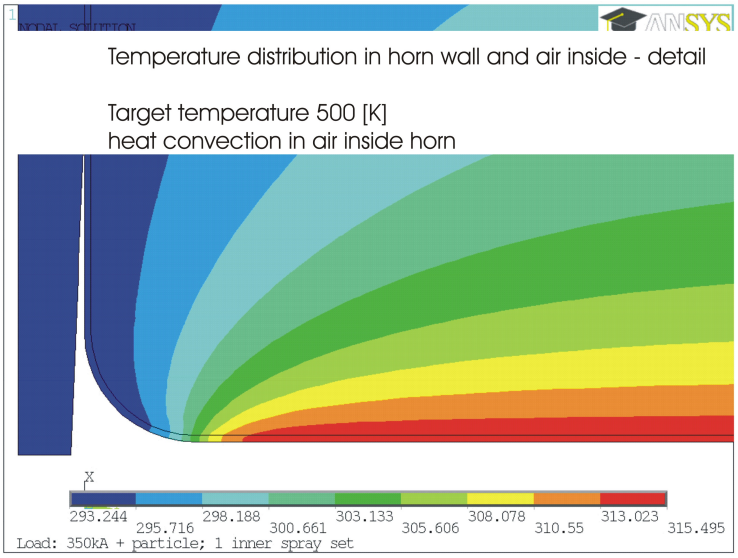

Figure 1.8: Temperature distribution in the horn wall and the air inside (admitted heat convection in air inside) - detail

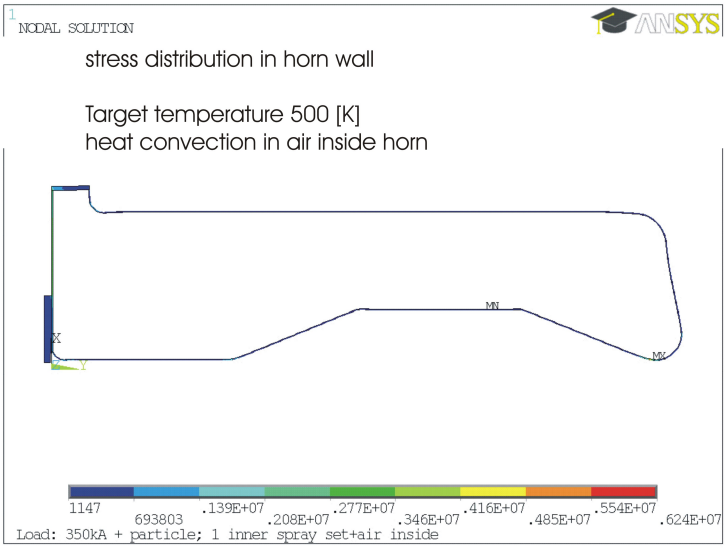

Figure 1.9: Equivalent stress distribution in the horn (heat convection in air inside admitted)

Chapter 2

Dynamic stress due to thermal and magnetic pulses

2.1 Horn geometry and the modelling approaches

This sections discusses the results of the analysis of the horn under the action of a sequence of pulses resulting from joule losses, secondary particle heating and magnetic pressure brought about by current pulses. The study of dynamic stresses is necessary in order to predict the fatigue life of the structure. The results will consider the horn configuration with a separated target, that was shown in Fig. 1.1 with the dimensions prescribed in Table 1.1.

2.2 Dynamic stress due to transient Joule heating

In the baseline scenario half-sine current pulses of magnitude 300–350 kA will be generated in the horn skin. These will result in Joule losses and an increase in temperature. Dynamic thermal stress will thus arise in the horn skin. The Joule losses have been estimated using analytical formulation. The Joule loss in the horn skin is calculated as:

$$P_{av} = RI_{RMS}^2 \tag{2.1}$$

$$I_{RMS} = \frac{I_0}{\sqrt{2}} \left(\frac{\tau}{T}\right)^2 \tag{2.2}$$

Here R is the resistance of a given horn section, and is obtained as follows:

$$R = \frac{\rho L}{2\pi r \delta} \quad \text{cylindrical shell} \tag{2.3}$$

$$R = \frac{\rho}{2\pi\delta}\frac{L}{r_2 - r_1}\ln\frac{r_2}{r_1} \quad \text{conical shell} \tag{2.4}$$

$$R = \frac{\rho}{2\pi\delta}\ln\frac{r_2}{r_1} \quad \text{annular plate} \tag{2.5}$$

where: ρ is the electrical resistivity, L is the length of the cylindrical or conical section (as specified in Table 1.1), and δ is the skin depth which for a harmonic signal of frequency f is calculated using the formula:

$$\delta = \sqrt{\frac{\rho}{\pi f \mu_0 \mu_r}} \tag{2.6}$$

Following [15], the skin depth for a sequence of half-sine pulses is taken to be that of a harmonic signal with frequency $f = 1/(2\tau)$, where τ stands for the pulse duration. For an aluminium alloy, for which the electric resistivity $\rho = 4 \cdot 10^{-8}\,\Omega$m, and for the pulse duration $\tau = 100\,6\mu$s, one finds for the skin depth the value:

$$\delta = 1.4\,\text{mm} \tag{2.7}$$

A more accurate approach to the calculation of the skin depth by expanding the sequence of half-sine pulses in Fourier series has been presented in [6].

The average Joule losses in different sections of the horn are shown in Table 1.2, for two current amplitudes: 300 kA and 350 kA. In Table 2.2 is included the power dissipated during the duration of a pulse, calculated using the expression:.

$$P_{pulse} = P_{av}\frac{T}{\tau} \tag{2.8}$$

The pulse duration τ has been taken to be 100μs and the seperation between the pulses $T = 1/12.5 = 0.08$ s.

The axisymmetric model of the horn with the prescribed mechanical boundary conditions is shown in Fig. 2.1. Adiabatic thermal conditions has been used in all the plots that follow.

Fig. 2.2 illustrates the distribution of the stress, calculated assuming that the maximum current is equal to 350 kA. The expanded region of maximum

Table 2.1: Average Joule losses

	Average power for max. current = 300 kA	Average power for max. current = 350 kA
Front face	0.53 kW	0.73 kW
Inner cond. cylinder 1	4.94 kW	6.72 kW
Inner cond. conical 1	1.32 kW	1.81 kW
Inner cond. cylinder 2	0.69 kW	0.93 kW
Inner cond. conical 2	1.35 kW	1.83 kW
Inner cond. cylinder 3	0.09 kW	0.12 kW
Outer conductor	0.93 kW	1.27kW
Exit face	0.31 kW	0.42 kW

Table 2.2: Joule losses per equivalent rectangular pulse, pulse duration = 100 s

	Power during pulse for max. current = 300 kA	Power during pulse for max. current = 350 kA
Front face	$0.43 \cdot 10^6$ W	$0.58 \cdot 10^6$ W
Inner cond. cylinder 1	$3.95 \cdot 10^6$ W	$5.58 \cdot 10^6$ W
Inner cond. conical 1	$1.06 \cdot 10^6$ W	$1.45 \cdot 10^6$ W
Inner cond. cylinder 2	$0.55 \cdot 10^6$ W	$0.75 \cdot 10^6$ W
Inner cond. conical 2	$1.08 \cdot 10^6$ W	$1.47 \cdot 10^6$ W
Inner cond. cylinder 3	$0.073 \cdot 10^6$ W	$0.1 \cdot 10^6$ W
Outer conductor	$0.75 \cdot 10^6$ W	$1.02 \cdot 10^6$ W
Exit face	$0.25 \cdot 10^6$ W	$0.34 \cdot 10^6$ W

stress is shown in Fig. 2.3. The maximum dynamic stress due to Joule heating is equal to 3.7 MPa (for the current pulse 350 kA) and (for the current 300 kA).

Figs. 2.4, 2.5 illustrate the temperature and stress plots vs. time at a selected point on the horn waist.

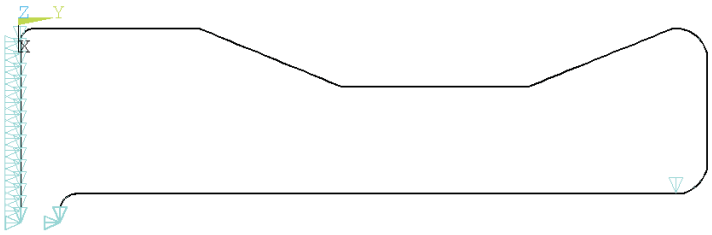

Figure 2.1: Model of the horn with the prescribed mechanical boundary conditions

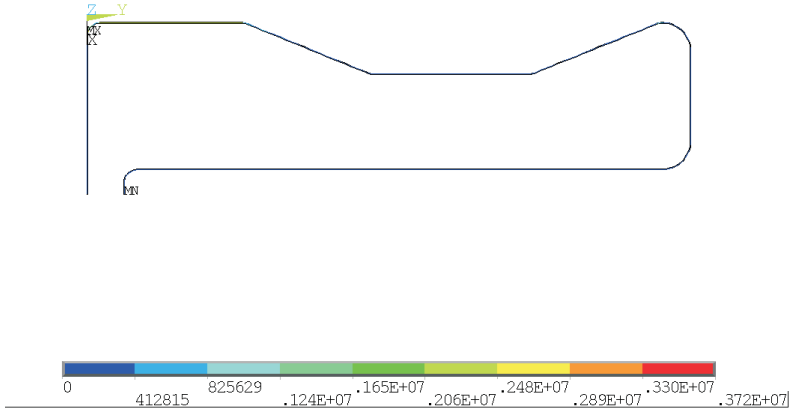

Figure 2.2: Distribution of the stress

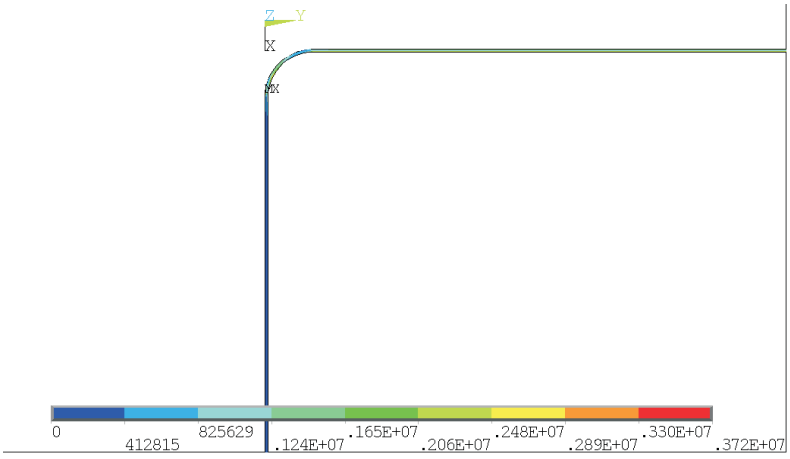

Figure 2.3: Expanded region of maximum stress

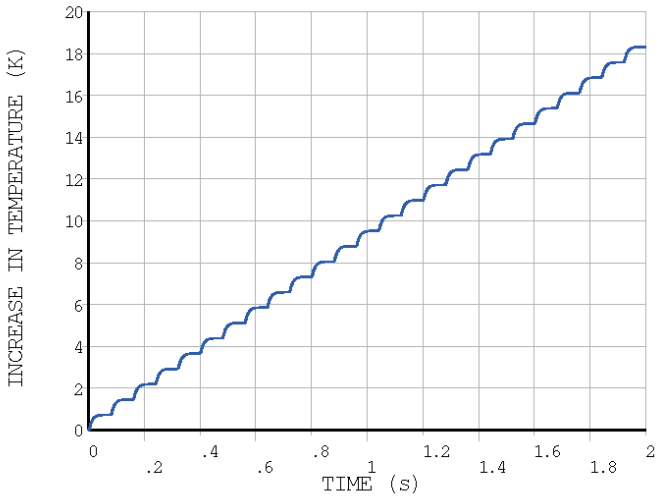

Figure 2.4: Temperature plot vs. time at a selected point on the horn waist

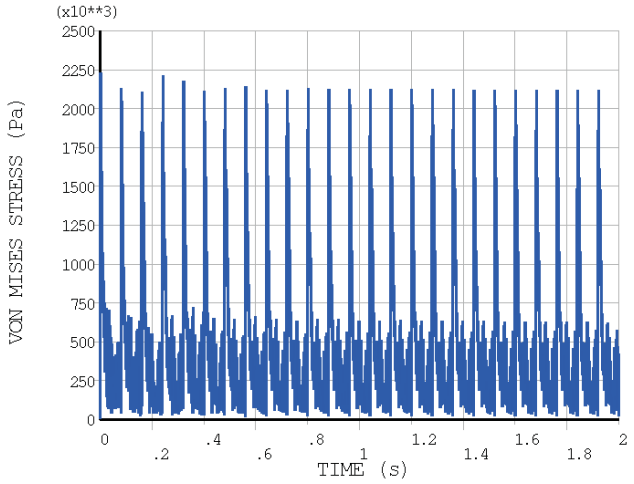

Figure 2.5: Stress plot vs. time at a selected point on the horn waist

2.3 Dynamic stress due to secondary particles

Secondary particles are absorbed in the horn during the beam pulse of 5μs duration. Dynamic thermal stresses resulting from the heating due to secondary particles have been calculated using the finite element method and are discussed below. The quasi-static effect of heat coming from the target embedded inside the horn has not been treated so far and is planned as the next step as part of the integration studies.
The power deposited in the horn skin has been calculated using Fluka by C.Bobeth and A. Longhin, and is specified in Table 2.3. These values correspond to the horn geometry as given in Table 1.1 and assuming a graphite target is embedded in the horn.

Table 2.3: Power deposited in the horn by secondary particles
pulse duration = 5 μs

	Average power	Power during equivalent rectangular pulse
Front face	0.76 kW	$12.2 \cdot 10^6$ W
Inner cond. cylinder 1	5.5 kW	$88 \cdot 10^6$ W
Inner cond. conical 1	1.76 kW	$28.1 \cdot 10^6$ W
Inner cond. cylinder 2	1.12 kW	$17.9 \cdot 10^6$ W
Inner cond. conical 2	0.58 kW	$9.28 \cdot 10^6$ W
Inner cond. cylinder 3	0.36 kW	$5.76 \cdot 10^6$ W
Outer conductor	3.34 kW	$53.4 \cdot 10^6$ W
Exit face	0.48 kW	$7.7 \cdot 10^6$ W

The distribution of the stress brought about by the secondary particles is shown in Fig. 2.6. The maximum value of the von Mises stress is about 3 MPa and it takes place at a point on the front face. A typical plot of the stress vs. time is shown in Fig. 2.7 , corresponding to a point on the horn waist. Apart from the dominant dynamic stress there is some quasi-static stress due to the temperature increase. The latter is small for the point being studied and the boundary condition where the horn downstream end is free to expand longitudinally.

2.4 Dynamic stress due to magnetic pulses - a simplified approach

Magnetic forces arise in the horn skin due to the current flowing through it. One approach to the structural response due to electromagnetic forces is by introducing the magnetic pressure [18]. Alternatively, coupled-field magneto-mechanical analysis can be used. The following results have been obtained using the first of the two approaches. In this method the action of the magnetic field in a thin horn, produced by the electric current is given by the formula [18]:

$$p = \frac{\mu_0 I^2}{8\pi^2 r^2} \tag{2.9}$$

where: I stands for the current and r is the radius. The magnetic forces that act on the horn unrestrained end can have an important effect on the

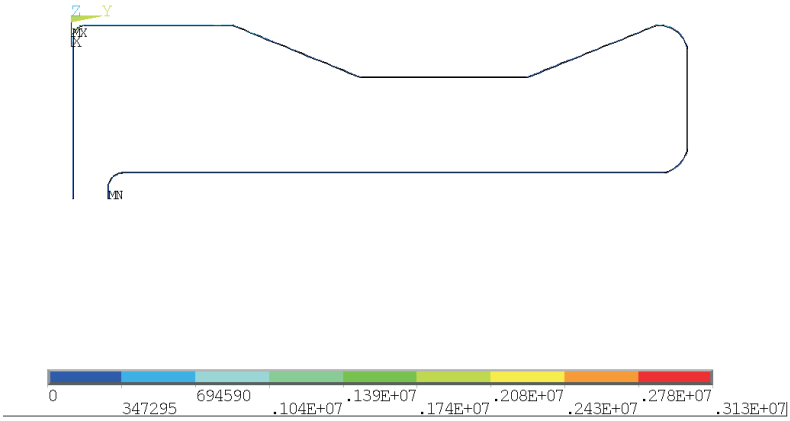

Figure 2.6: The distribution of the stress brought about by the secondary particles

calculated stress levels, as discussed in [7]. For the end plate the magnetic pressure is perpendicular to the plate surface and depends is a function of the distance from the horn axis according to formula .
Equivalent rectangular magnetic pressure pulses have been used in the analysis instead of half-sine pulses. The value of the pressure of the rectangular pulse is obtained by making the impulse of the equivalent rectangular pulse equal to that of a half-sine pulse of the same duration. Thus the pressure in Eq. 2.9 is multiplied by $2/\pi$.
The magnetic pressure of an equivalent rectangular pulse is shown in Fig.2.8, assuming that the maximum current is equal to 350 kA. Fig. 2.10 shows the stress distribution at the time instant when stress assumes its maximum value. The maximum stress due to the magnetic forces is 41 MPa and for the present baseline Superbeam horn geometry it has the biggest contribution to the overall stress in the horn skin.
Figs. 2.11 illustrate the time plots of the stress at a point on the horn waist, respectively, for a single pulse and a sequence of 25 pulses.

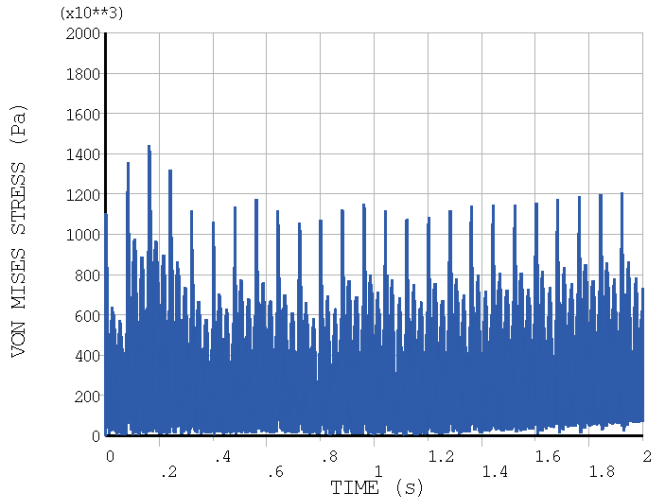

Figure 2.7: Stress vs. time corresponding to a point on the horn waist

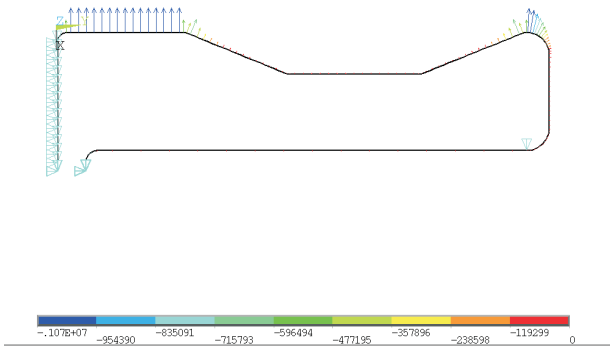

Figure 2.8: Magnetic pressure of an equivalent rectangular pulse (maximum current 350kA)

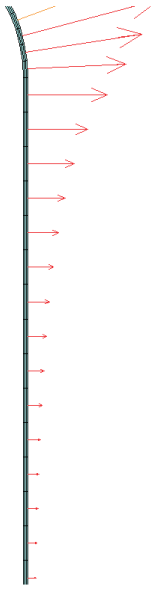

Figure 2.9: Magnetic pressure of an equivalent rectangular pulse (maximum current 350kA) - detail

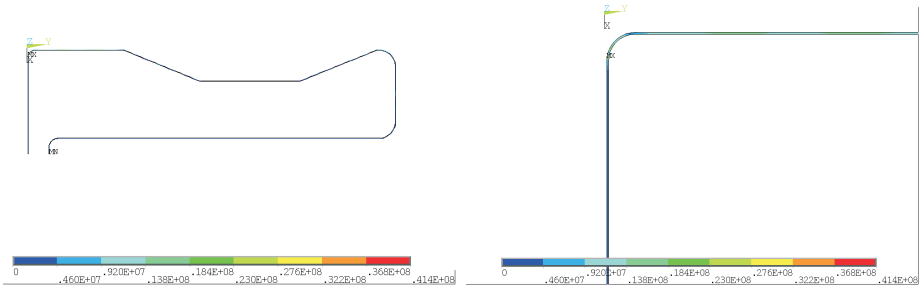

Figure 2.10: Stress distribution at the time of its maximum value

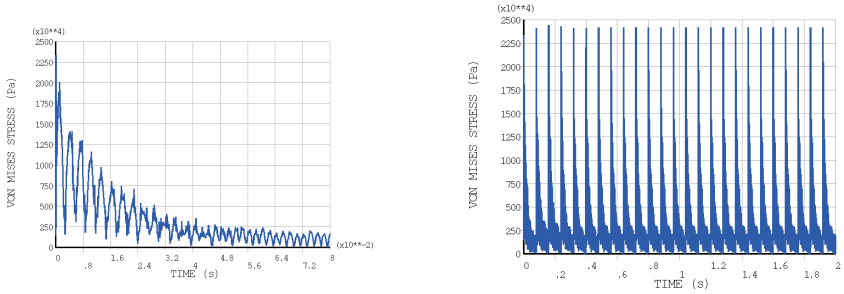

Figure 2.11: Stress vs time plot, at a point on the horn waist, for a single pulse and a sequence of 25 pulses.

2.5 Dynamic stress due to magnetic pulses - coupled magneto-solid analysis

The analysis in the previous section was approximate, since the magnetic forces were modelled by analytical expressions of magnetic pressures. These expressions were valid for a cylindrical geometry and an annular plate. This section describes the results obtained using a more accurate coupled magneto-solid analysis of a horn. For this type of numerical analysis the revised shape of the horn with the spheroidal end plate instead of the flat one is used.

The first model created for the coupled magneto-solid dynamic analysis was a complete horn design including the surrounding air. The main drawback of this model was the large number of elements used, which greatly influenced both the number of equations to be solve, as well as the computation time. In order to reduce the size of the problem, only a wedge-shaped fragment of the horn with certain symmetry boundary conditions is used for the computation. This approach is made possible due to the axisymmetric shape of the horn.

The solution to the coupled field problem is obtained using transient analysis. At first, the half sine current pulses of duration $t_1 = 100\mu s$ are applied to the modelled horn, at the intervals of $t_2 = 8ms$. This allows for the magnetic vector potential and current density distribution to be calculated, for each step of the analysis. From these results, other values such as magnetic flux density or magnetic forces, can be derived. The magnetic forces are then transferred onto a structural model in order to calculate the resulting stresses and displacements. It is assumed that the effect of the structural deformations on the

magnetic field is negligible, thus allowing for one-directional load transfer.

In order to ascertain the correctness of the calculations, several simpler magnetic numerical models such as a coaxial cable or a cylinder were created and evaluated. Additionally, in case of the dynamic current excitation, the distribution of the current density throughout the conductor is not constant, but depends greatly on the frequency of the current. This behaviour, known as "skin effect" is included in the computation. The comparison between the analytical and numerical solution shows that the results are similar.

2.5.1 Boundary conditions

The magnetic analysis requires the model to be subjected to the following boundary conditions:

- flux-parallel condition on the external surfaces (limiting the magnetic flux to the enclosing air volume)
- coupled voltage for the current inlet nodes, as well as zero voltage for the current outlet nodes (thus specifying the current flow direction)

In case of the structural analysis the conditions include:

- cantilever clamping of the model (restrictions imposed on displacement at the base of the horn)
- symmetry conditions on both sides of the wedge shape

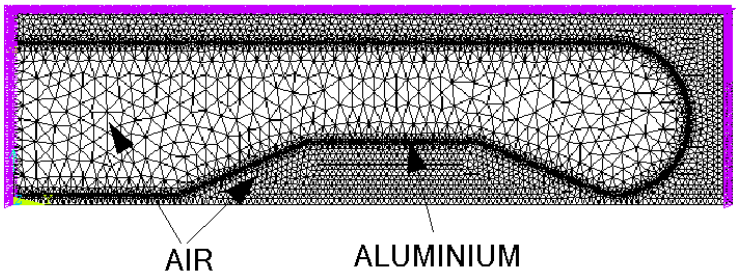

Figure 2.12: Magnetic horn model

2.5.2 Results of the coupled analysis

The results show the magnetic flux density and current density across the depth of the cylindrical part, for the horn excited by sinusoidal and impulse current. The structural response of the horn to this excitation can be seen in Fig.2.17 and 2.18, where the highest displacements and stresses are given. The maximal stress magnitude from the magnetic forces generated by the sine-wave pulses of amplitude $I_a = 300[kA]$ is around 32 MPa. With the amplitude I_a increased to the value of $350[kA]$ the resulting maximal stress intensity is 43 MPa. The results which are obtained using the coupled field analysis are similar to the ones obtained through the simplified approach, as shown in Table 2.4

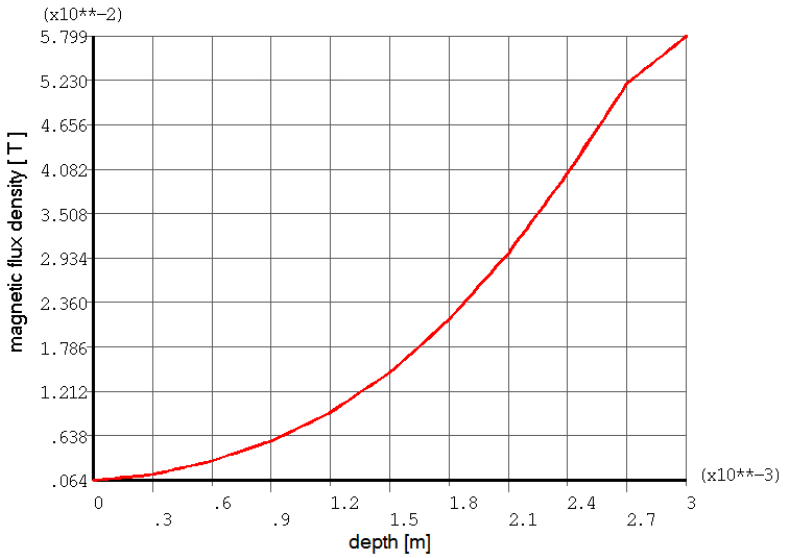

Figure 2.13: Magnetic flux density [T] across the depth of the cylindrical part of the horn for the sinusoidal current excitation

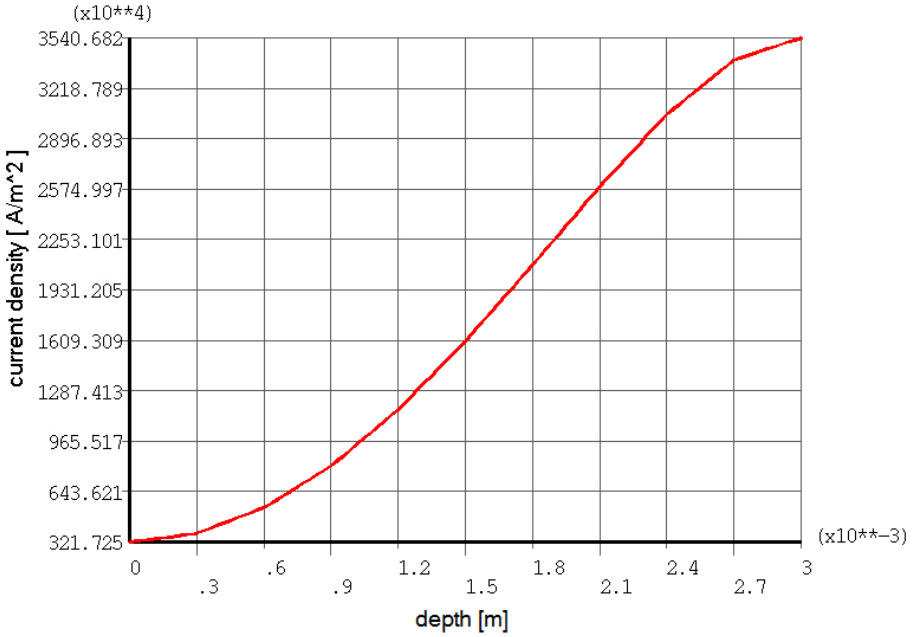

Figure 2.14: Current density [A/m^2] across the depth of the cylindrical part of the horn for the sinusoidal current excitation

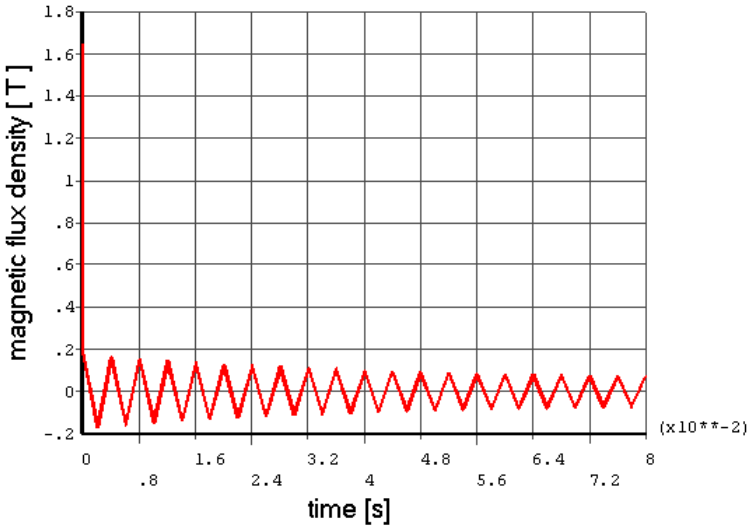

Figure 2.15: Magnetic flux density [T] at the selected node of the spheroidal end plate for the half-sine pulse current excitation

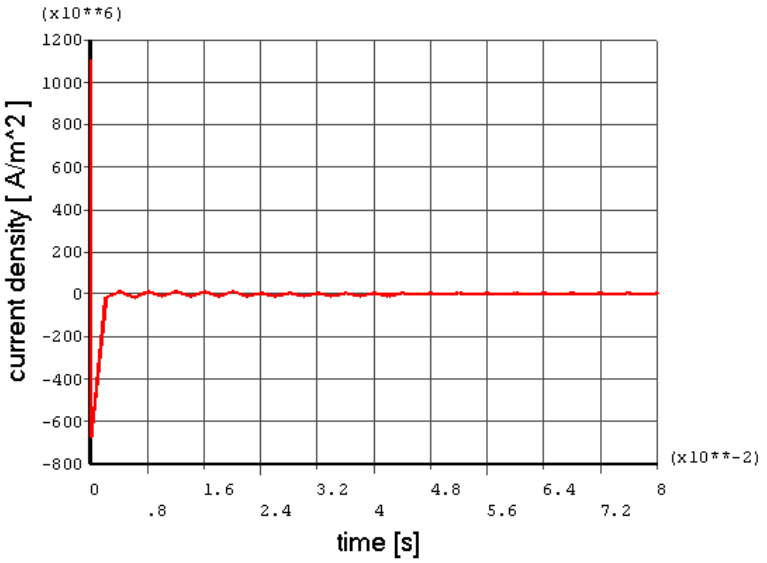

Figure 2.16: Current density [A/m^2] at the selected node of the spheroidal end plate for the half-sine pulse current excitation

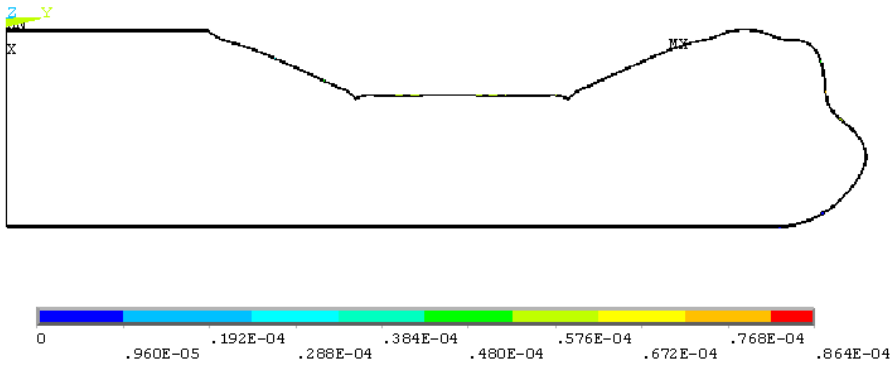

Figure 2.17: Highest displacements [m] in the model (half-sine pulse current excitation - 350kA)

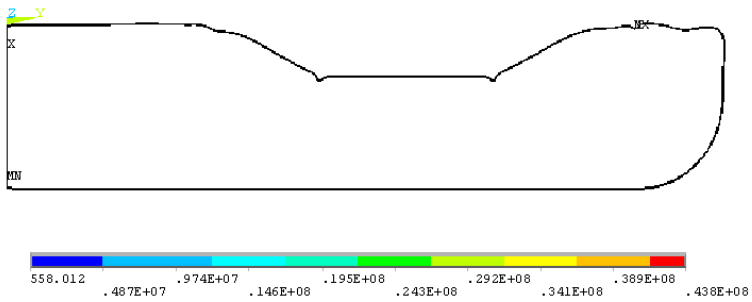

Figure 2.18: Highest stresses [Pa] in the horn (half-sine pulse current excitation - 350kA)

2.6 Conclusions

The summary of the dynamic stress levels calculated at different conditions is provided in Table 2.4

Table 2.4: Summary of the dynamic stresses

Stress due to Joule heating	3.7 MPa (at 350 kA) 2.7 MPa (at 300 kA)
Stress due to secondary particle heating	3.1 MPa
Stress due to magnetic forces - simplified analysis	41 MPa (at 350 kA) 30 MPa (at 300 kA)
Stress due to magnetic forces - magneto-solid analysis	43.8 MPa (at 350 kA) 32.2 MPa (at 300 kA)

The dynamic stress levels superimposed on the quasi-static stress are the basis of the fatigue life estimate of the horn. The approach to the fatigue life estimate and very preliminary results have been discussed in [6].
The analysis of this and the previous section is now being extended to include the target embedded inside the horn with a view to developing the concept of an integrated horn-target system.

Chapter 3

Fatigue life estimation

3.1 Introduction

The realistic mechanical structures, or their parts, are commonly subjected to repeated loads, which are also named as cyclic loads. As the results of their action, there are obtained the cycle stresses, which can lead to physical material damage. Even at stresses below the ultimate strength, the microscopic damages can accumulate in the form of crack or the other form of macroscopic damage that leads to failure of the element. This process of damage and failure due to cyclic loading is called as fatigue [8]. Due to characteristic features of applied methods and the level of complication, the fatigue analysis is understood as an independent part of the strength of materials. The complexity of the analysis comes from the existences of many components, which have an important view on their results. Let us briefly classify them:

- Design of experimental tests: estimation of uniaxial S-N curves, estimation of multiaxial (biaxial) S-N curves, probabilistic (statistical) approach.
- Method of analysis: stress-based approach, strain-based approach, crack propagation method / fracture mechanics (Griffith criterion, crack opening displacement - COD, J-integral).
- Zones on the S-N curve (existence of the plastic strains regions) - fatigue strength: quasi-static, low-cycle, high-cycle.
- Methods of description of non-symmetric cycles - diagrams of: Smith, Haigh, Heywood; equivalent completely reversed stress.

- Methods of description of multiaxial stress: effective stress amplitude, effective mean stress.
- Description of the cumulative fatigue damage: methods of: Palmgren-Miner, Serensen, Haibach, Henry, Corten-Dolan, and the other ones.
- Methods of description of the realistic construction's effects of: geometry (notch effect, size effect), material machining (cutting, welding etc.), surface (surface roughness, changing of surface properties, residual stress, corrosion), material structures (thermal machining, residual stress).
- Methods of determination of the environmental effects: stress amplitude, thermal loadings, frequency and stress form, corrosion, freeting, prestressing.
- Methods for estimation of the material damage due to irradiation (see B.Skoczen).

Vibration of engineering structures produces time variable displacements functions. Hence, the components of stress tensor are time function too. The form of vibrations is determined by structure geometry and applied boundary conditions. They determine the modal characteristic of the system. For complex structures relatively high modal density is often observed. The other important parameter influencing the solution is the type of external excitation, and its spectrum in particular. For short time excitation, as pulses, the relatively broad frequency band of excitation is observed. The most important role plays values of natural frequencies of the system. Thus often in the transient case, the time history of displacements and stress components have irregular form with respect to time. It means that the vibrations have the form of quasi periodic vibrations. But they are still not of random type from nature of the process (if not chaotic ones). The known in literature fatigue analysis of such cases can generally takes the following form:

- Analysis in time domain superposition of harmonically variable stress components (e.g. Dowling [8]).
- Cycle counting of irregular stress functions in time domain (e.g. rain-flow method [8]).
- Spectral method in frequency domain based on PSD analysis (e.g. Lagoda [16]).

- Spectral method in frequency domain based on FFT analysis (Kozień, Szybiński [10]).

3.2 Theoretical basis of the cycle counting in general cases

3.2.1 Multiaxial, broadband stress

For real engineering structures, the cyclic loading are commonly the source of complex states of stress, known as multiaxial stresses. The experimental fatigue curves are usually determined for the uniaxial cases. For such cases it is possible to make direct fatigue analysis based on experimental data or apply known in literature theoretical methods of describing its interaction. An additional complexity is that the different sources of cyclic loading may vary in phase or in frequency. Therefore, in general, the problem of finding the equivalent uniaxial cycles of stress arises. Moreover, due to the fact that the fatigue curves are investigated for some characteristic cycles forms, the uniaxial stress should be transformed to the required one, usually of completely reversed type.

3.2.2 Effective stress amplitude and effective mean stress

The fracture criterion parameter is commonly applied in strength material analysis to estimate the level of structure exertion. There are several, well known, hypothesis of material exertion, known as fracture criterion. The mechanism of plastic deformation and mechanism of fatigue failure are not the same. Therefore, there are no simple reasons for application of the fracture criterion approach for fatigue. However, due to the fact of non existence the other useful estimator, often the same concept of equivalent stress is applied in fatigue analysis to transform amplitudes of the multiaxial stresses into the uniaxial case. The most common formula is the application of von Mises equivalent stress σ_{VM} (3.1).

$$\sigma_a = \frac{1}{\sqrt{2}}\sqrt{(\sigma_{1a} - \sigma_{2a})^2 + (\sigma_{2a} - \sigma_{3a})^2 + (\sigma_{1a} - \sigma_{3a})^2} \tag{3.1}$$

The effective mean stress like the effective stress amplitude can be estimated by applying the definition of equivalent von Misses stress in the above form. But for such a case the different effect of mean tension versus mean compression

in relation to fatigue is not included. It has been taken into account in Sines' empirical expression (3.2) for effective mean stress, where a is an empirical factor. The equation was simplified by Fuchs and Stephens, by putting the a factor as equal to unity [9]. The new formula is sometimes named as the Sines equivalent stress.

$$\sigma_m = a(\sigma_{1m} + \sigma_{2m} + \sigma_{3m}) \tag{3.2}$$

3.2.3 Equivalent completely reversed stress

The experimental S-N curve is usually constructed for the one of the characteristic stress changes in time. The most popular is the completely reversed stress cycle. The following values are not independent: stress amplitude, equivalent completely reversed stress, mean stress, yield stress and ultimate stress. There are some, well known in literature formulas, which can be applied to describe relationships between the mentioned above parameters. The commonly used in practice formulas are as follow: linear Soderberg or linear Goodman, nonlinear Gerber or the Smith, Watson and Topper (sometimes called as the SWT). Based on the Goodman hypothesis, for any harmonically varying cycle of stresses it is possible to determine the equivalent completely reversed stress in the form (3.3), where σ_u - ultimate stress [8].

$$\sigma_{ar} = \frac{\sigma_a}{1 - \frac{\sigma_m}{\sigma_u}} \tag{3.3}$$

3.2.4 Cycle counting, cumulative damage

The response of excited vibrating mechanical system is described by set of frequencies, for which the stresses can vary in time. These frequencies are the natural frequencies of the system. The spectrum of loading/stress has in general an irregular form. The fatigue life in spectrum loading is a function of accumulated effects in analyzed part, at various stress levels, throughout its performance, that is, the function of cumulative damage [8]. Such formulated problem is not easy to describe, and there are many known in literature methods of analysis. The most popular is the Palmgren-Miner assessment. Some others are the generalized idea of Palmgren-Miner rule (e.g. Serensen, Haibach, Corten-Dolan).

For completely irregular histories of loads/stresses with time, the problem of identification of cycles arises. The most commonly used method is the rain

flow counting.

3.2.5 Spectral method in frequency domain based on FFT analysis

In dynamic process the stress components are functions variable in time and usually have the irregular form. The question is: how to determine and then to count the component cycles. If excitation has the form of harmonic type, the response of vibrating structures depends of their natural frequencies and excitation frequency. If excitation is a pulse type, the response depends only on the natural frequencies of the system. Therefore in frequency domain the stress function has a discrete representation. It means that with every frequency existing in spectrum, the suitable value of stress amplitude is connected. Moreover, the excited stress function in time domain has usually the zeroes mean value. Therefore if the FFT transform of the stress function is known, and it has the form of peak-like form, it seems that the function can be represented as a sum of suitable harmonic functions. So, it is the attempt to a form of the FFT based cycle-counting for considered time period. If the components are in phase it can be amplified for some time points. For simplicity and safety, it is assumed further that the components are in phase.

Therefore it is assumed that vibrations has the average value of vibration stress for each component and a total sum are zeroes. If there are any other types of static-type stress they can be applied in the form of the mean stress in formula (3.3).

Let us assume that in the FFT amplitude characteristic there are N, non-zeroes (or sufficiently high for fatigue analysis) bars for frequencies f_i (i=1,...,N) with stress amplitude values σ_{ai}. Then the following set of the following parameters are defined: the cycle number parameter n_i and the equivalent stress amplitude value σ_{ai} (i=1,...,N). [10].

Finally for the lowest frequency f_1 (and the longest repetition period T_1 connected with the considered frequency) it is obtained the following pairs of parameters (number of cycles, stress amplitude) (n_i, σ_{ai}). This is the base for further fatigue analysis, based on the Palmgren-Miner concept.

3.2.6 Spectral method in frequency domain based on PSD analysis

The analysis is base on application of the power spectral density function (PSD) fot the time history stress functions. The application of the method is

divided in the following steps [16]:

- Calculation of the stress functions in time domain.
- Calculation of the PSD matrix.
- Determination of critical plane or choosing of the dangerous point in structure.
- Determination of the equivalent PSD function for chosen point.

$$G_{eq}(f) = \sum_{i,j=x,y,z,i\neq j} Q_{ij} G_{\sigma_i \sigma_j}(f) \tag{3.4}$$

$$Q_{ij} = \begin{bmatrix} 1 & -0.5 & -0.5 & 0 & 0 & 0 \\ -0.5 & 1 & -0.5 & 0 & 0 & 0 \\ -0.5 & -0.5 & 1 & 0 & 0 & 0 \\ 0 & 0 & 0 & 3 & 0 & 0 \\ 0 & 0 & 0 & 0 & 3 & 0 \\ 0 & 0 & 0 & 0 & 0 & 3 \end{bmatrix} \tag{3.5}$$

- Determination of statistical moments.

$$\left.\begin{aligned} p(\Delta\sigma) &= \tfrac{1}{2\sqrt{k_0}}[\tfrac{G_1}{Q} e^{\frac{-Z}{Q}} + \tfrac{G_2 Z}{R^2} e^{\frac{-Z^2}{2R^2}} + G_3 Z e^{\frac{-Z^2}{2}} \\ Z &= \tfrac{\Delta\sigma}{2\sqrt{k_0}} \\ G_1 &= \tfrac{2(x_k - I^2)}{1+I^2} \\ G_2 &= \tfrac{1-x_k-G_1^2}{1-R} \\ G_3 &= 1 - G_1 - G_2 \\ R &= \tfrac{I-x_k-G_1^2}{1-I-G_1+G_1^2} \\ Q &= \tfrac{1.12(I-G_3+G_2 R}{G_1} \\ x_k &= \tfrac{k_1}{k_0}[\tfrac{k_2}{k_4}]^{0.5} \\ I &= \tfrac{k_2}{\sqrt{k_0 k_4}} \\ k_n &= \int_0^{+\infty} G(f) f^n \, df \end{aligned}\right\} \tag{3.6}$$

- Calculation of fatigue life.

$$T = \frac{1}{\sqrt{\frac{k_4}{k_2}} \int_0^{+\infty} \frac{p(\Delta\sigma)}{N_f(\Delta\sigma)}\, d\Delta\sigma} \tag{3.7}$$

3.3 Life time analyses

3.3.1 CERN NuFACT short horn

The geometry of analysed structure is shown in Fig.3.1, as a suitable cross-section. The enclosed plot is a horn version on 15/05/2001. Geometry of the horn has been a little changed, and it has been taken into account in FEM model, as a version on 15/09/2001. The structure is axisymmetric. The magnetic field is generated by currant flow of pulse form. It has a form of sequence of half-sine pulses with time duration of 93 ms, repeated every 20 ms (50 Hz), with amplitude of 400 kA. The requested number of pules is equal to repetitions, i.e. five months of operation.

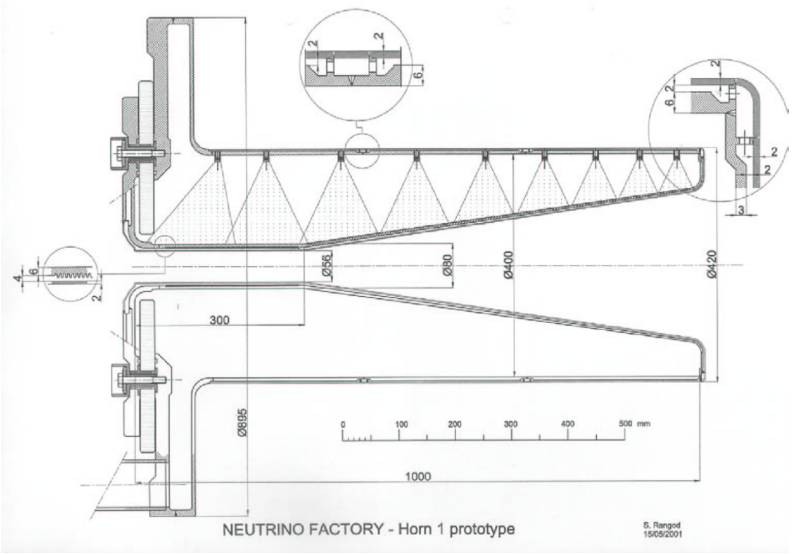

Figure 3.1: CERN Horn NuFACT

The Horn is made of aluminum alloy 6082-T6, which S-N curve is shown in Fig. 3.2.

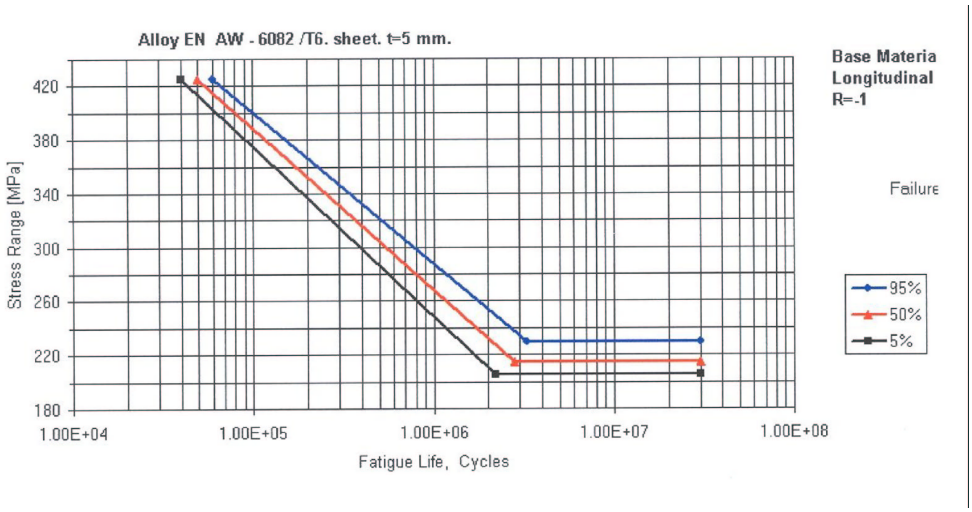

Figure 3.2: S-N curve for aluminum alloy 6082-T6

The analysis of dynamical behaviour of a structure is based on the finite element modelling of the structure. Due to almost axisymmetric geometry, and axisymmetric excitation (magnetic force), the FEM analysis has been done as an axisymmetric one, by applying the Ansys solid 42 type elements. Only the solid structure, without cooling medium (water) has been modelled. The model contains of 1666 elements. The boundary conditions have been applied as the fixed ones (UX=UY=0), for all nodes around the main mounting screws (placed on the left set of plates, with distance from the axis between 200 and 210 mm).

Estimation of thermal stresses has been done in the static case, as a result of thermal elongation under assumed temperature distribution. The gravity effect was not taken into account. Nodal temperature values come from the thermal estimation given in [15]. The temperature distribution is assumed to be linearly varying vs. radius (distance from the axis), between fourth characteristic points:

- The radial end, $R = 0.4475$ m - 20°C,
- The outer line, $R = 0.210$ m - 25°C,

- The internal corner in the right end, $R = 0.140$ m - 40°C,
- The internal corner in the left end, $R = 0.0028$ m - 70°C

The results of the analysis show that the most dangerous region of the structure is the internal corner in the left end. The equivalent Tresca stresses reach dangerous values of 225 MPa. Out of the mentioned area, the equivalent Tresca stress rapidly goes down.

The structure response in time domain must be analyzed in the transient case. It is due to short pulse length and relatively short distance between pulses having in mind the dynamic characteristics of the structure (lowest natural frequency of 107.7 Hz, modal damping ratio 0.004). The external exciting force has the form of magnetic type coming from the currant flow. It acts on the whole body of the structure, but can be simplified as the surface, pressure-like force, acting on the internal surface of the conductor. Due to geometry of the horn, the pressure values can be estimated from the simplified formula 3.8, where: I_0 - current, R - distance of the suitable middle surface point from the HORN axis. The magnetic pressure is varying in time domain in the same way as the currant flow.

$$p = I_0^2 \frac{\mu_0}{8\pi^2 R^2} \tag{3.8}$$

The stress distribution in the structure has the form of multiaxial ones. The standard S-N fatigue curves are used for uniaxial and usually alternate stress (Fig. 3.2). Therefore the equivalent completely reversed uniaxial stress parameter (3.3) must be analysed. Analysis of obtained values of dynamic stress distribution in time domain and static thermal stress have made possible to choose the most danger regions in the structure. The obtained values of the equivalent completely reversed stresses show, that the structure can work on safety level about 1.63 with number of cycles of (experimental S-N curves, assumption of the completely reversed bending nature of stress variation). But, as it has been shown, in realistic structures dynamic stresses may growth up with number of generated pulses. Therefore, it is recommended to increase the structure modal damping coefficient.

3.3.2 EUROnu horn

Estimation of life time for EUROnu horn was made for preliminary estimated thermal stress and dynamic stress coming only one magnetic pulse response. In FEM simulation there was no observed effect of stress and displacement increasing in time. Time-history of the highest stress component is shown in Fig. 3.3 for one pulse, and in Fig. 3.4 for sequence of pulses.

The equivalent thermal stress are assumed to be equal to 102.5 MPa. Life time prediction were estimateed for three models of probability density: Rayleigh, Dirlik and Benasciuutti-Tovo. Moreover each estmation were made for three values of probability for S-N curve (Fig. 3.2). The estimated valules of time (in seconds) are given below. Remember, that number of pulses per second is equal to 12.5.

Table 3.1: Life time estimation.

S-N CURVE PROBABILITY	LIFE TIME [s]
95 %	$8.6 \cdot 10^7$
50 %	$1.9 \cdot 10^7$
5 %	$6.6 \cdot 10^6$

3.4 Corrosion fatigue

Under conditions of simultaneous cyclic stressing and corrosion, the reduction in strength is greater than the additive effects of the separate processes. Although it is possible to provide the adequate protection for metallic parts, which are stressed under static conditions, most surface films (including naturally protective oxides) can be more easily broken down or disrupted under cyclic loading. In general however, the fatigue strength of material in a particular corrosive medium can be related to corrosion resistance of the materials in that medium [1]. Even relatively mild corrosive atmospheres can reduce the fatigue strength of aluminium structures compared to the fatigue strength in dry air [1]. Under conditions of corrosion fatigue all types of aluminium alloys exhibit about the same percentage reduction in strength when compared with their fatigue in air [1].

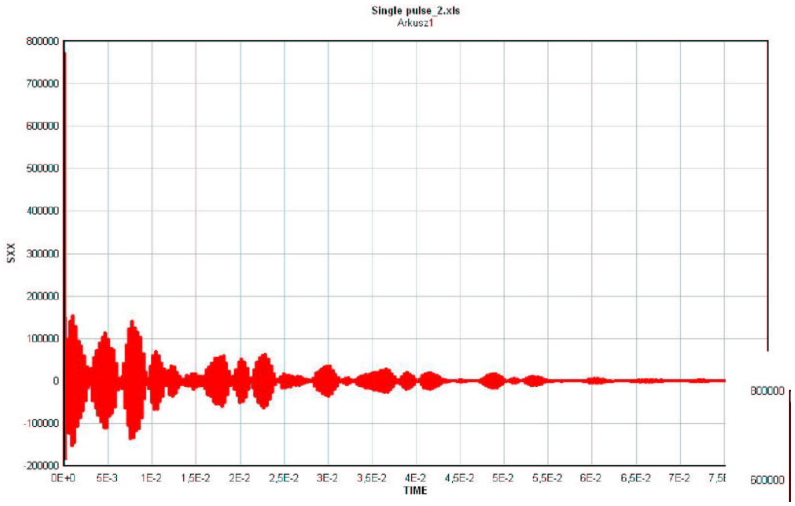

Figure 3.3: Response of structure for one magnetic pulse σ_{xx} component.

Fatigue strength of aluminum alloys are lower in such corrosive environments as seawater and other salt solutions than in air, especially when evaluated by low-stress low-duration tests. However such corrosive environments produce smaller reductions in fatigue strength in the more corrosion-resistant alloys, such as the 6xxx series [14].

3.5 Influence of welding

Analysis of welding process and welding effects are not a topic of this report. However, due to necessity of application of this process in production, chosen important remarks are given below according to EUROCODE 9 [3]:

- The welding process MIG is preferred, and TIG one is allowed only for thickness up to 6 mm and for repair.
- For the welded structures made of the aluminium 6082, the following filler metals are preferred (the given order is importantm): 5356, 5183, 4043.
- The heat-affected zones (HAZ) are the regions about ± 20 mm along line of welding for the MIG process and thickness less than 6 mm.

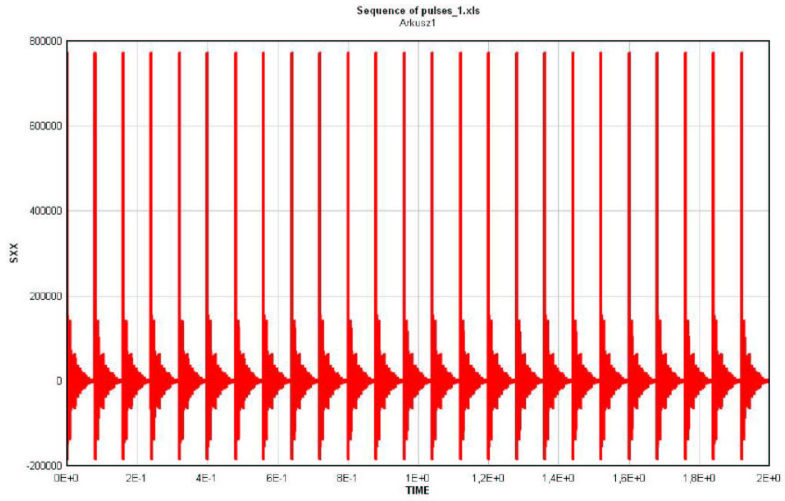

Figure 3.4: Response of structure for sequence of magnetic pulses σ_{xx} component.

- The ultimate strength of metal for aluminium 6082T6 is equal to given value multiplied by softening factor ρ_{HAZ}. The value of ρ_{HAZ} is equal to 0.65 for the MIG process, and to 0.5 for the TIG one.

Generally the welds in AlMgSi alloys have good resistance to corrosion. But in some corrosive environments localised corrosion can occur. Possible sites for crevice corrosion and possible weld defects that might lead to subsequent corrosion process are discussed in [2]. Therefore the welding process must be done carefully and with high quality.

Chapter 4

Degradation of material properties due to radiation

The EuroNu Super Beam project requires the beam power of 4 MW. As the target is embedded within the bore of a conventional pulsed current magnetic horn, the cylindrical portion of the horn located in direct proximity of the target is exposed to high level irradiation. In order to predict the lifetime of the horn, subjected to combination of irradiation and mechanical loads, a dedicated algorithm has been developed. The algorithm is based on the following assumptions:

1. cylindrical portion of the horn is studied,
2. target is located coaxially inside the horn cylindrical part,
3. the profile of dpa in the horn cylindrical wall and in the target are similar,
4. single cycle is composed of beam deposition in the target, production of radiation induced damage (dpa) and mechanical compression (heating) and traction (cooling) of the horn wall,
5. the horn is made of aluminium and its properties w.r.t. irradiation are accounted for,
6. evolution of radiation induced damage occurs due to mechanical loads (compression/traction),
7. the accumulated damage in the horn wall increases with each beam deposition in the target (each cycle).

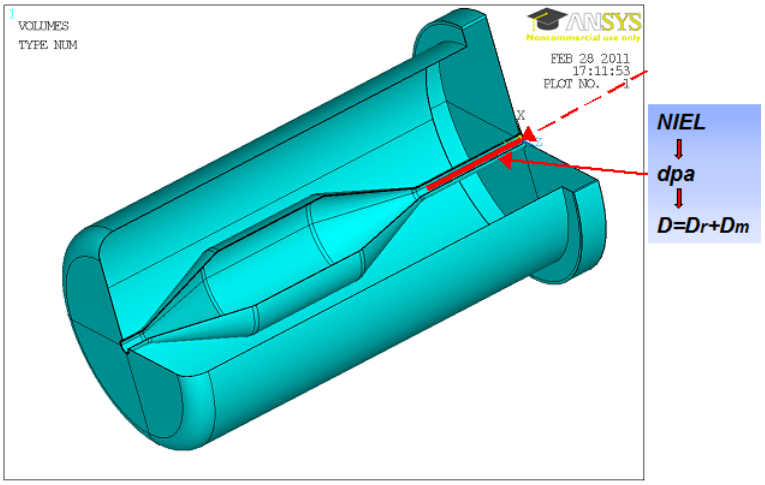

Figure 4.1: Target/horn configuration for the EuroNu Super Beam.

Distribution of the beam deposited power in [kW/cm3] in the target (Be, C, Al, AlBeMet) has been shown in Fig. 24 of the previous report on The target and horn for the SPL-based Super Beam: preliminary design report. Assuming that the flux of secondary particles, emitted from target to horn, and the related distribution of NIEL (non-ionizing energy loss) in the cylindrical part of the horn will be proportional to the beam deposited power in the target, the following typical dpa distribution in the horn cylindrical tangent is postulated (Figure 4.2):

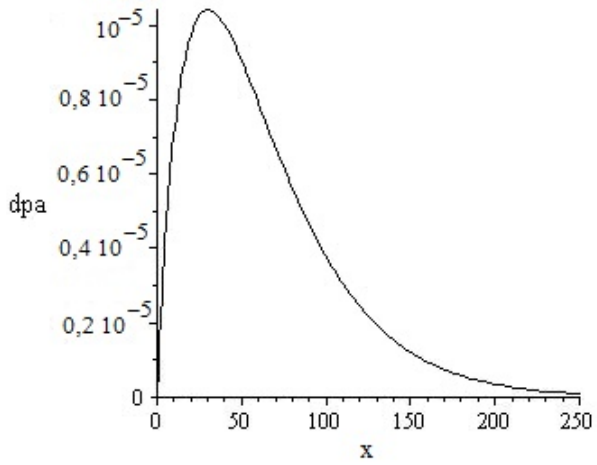

Figure 4.2: Postulated typical distribution of dpa in the horn cylindrical tangent.

Here, the indicated length of the cylindrical tangent has been cut off at 250 mm for practical reasons and the maximum dpa is of the order of 10^{-5}. The dpa corresponding to the length higher than 250 mm is negligible when compared to the values obtained below 250 mm. Typical dpa distribution has been described by the following function:

$$dpa = ax^b e^{cx} \tag{4.1}$$

Based on the known dpa distribution the density of defects (clusters of voids) caused by irradiation is computed:

$$q_c = \begin{cases} C_{qI}(dpa)^{n_{qI}} & \text{for} \quad dpa < D_s \\ C_{qII}(dpa)^{n_{qII}} & \text{for} \quad dpa \geq D_s \end{cases} \tag{4.2}$$

or

$$q_c = \begin{cases} C_{qI} a x^{b n_{qI}} e^{c n_{qI} x} & \text{for} \quad dpa < D_s \\ C_{qII} a x^{b n_{qII}} e^{c n_{qII} x} & \text{for} \quad dpa \geq D_s \end{cases} \tag{4.3}$$

Here, D_s denotes the threshold value. The following clusters of voids density distribution has been obtained for the cylindrical tangent of the horn:

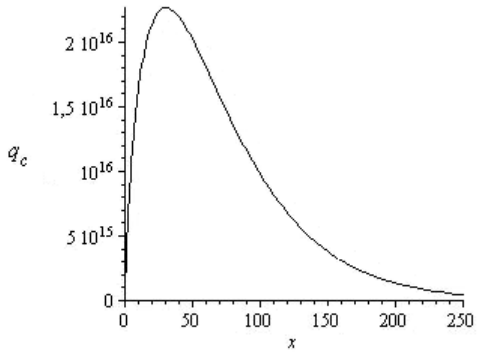

Figure 4.3: Clusters of voids density distribution along the horn cylindrical tangent.

In the same way the radius of clusters is computed. Here, the following formulae are applied:

$$r_c = \begin{cases} C_r(dpa)^{n_r} & \text{for} \quad dpa < D_s \\ r_{cr} & \text{for} \quad dpa \geq D_s \end{cases} \tag{4.4}$$

or

$$r_c = \begin{cases} C_r a x^{bn_r} e^{cn_r x} & \text{for} \quad dpa < D_s \\ r_{cr} & \text{for} \quad dpa \geq D_s \end{cases} \tag{4.5}$$

Hence, the distribution of radius of clusters along the horn cylindrical tangent is illustrated in Fig.4.4.

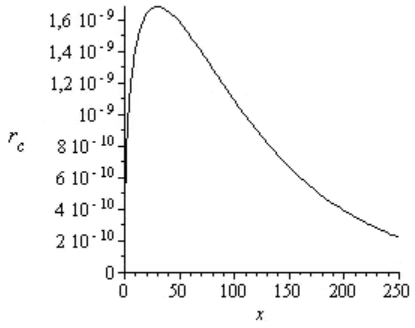

Figure 4.4: Radius of clusters of voids as a function of distance along the horn.

Based on the above functions, the "surface" density of clusters of voids is computed by means of the following formula:

$$q_A = {q_c}^{2/3} = \begin{cases} (C_{qI} a x^{bn_{qI}} e^{cn_{qI}x})^{2/3} & \text{for} \quad dpa < D_s \\ (C_{qII} a x^{bn_{qII}} e^{cn_{qII}x})^{2/3} & \text{for} \quad dpa \geq D_s \end{cases} \tag{4.6}$$

The surface density of clusters of voids along the horn cylindrical tangent is shown in Figure 4.5.

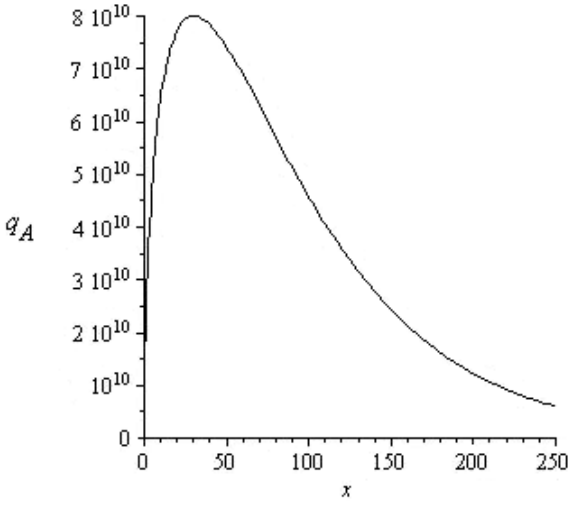

Figure 4.5: Surface density of clusters of voids along the horn cylindrical tangent.

Here, also the portion of 250 mm of the horn cylindrical tangent has been shown. The surface density of clusters of voids has been recalculated in order to obtain the damage parameter D_{r0}, according to the following formulae:

$$D_{r0} = q_A \pi r_{c0}^2 \tag{4.7}$$

$$D_{r0} = {q_c}^{2/3} = \begin{cases} (C_{qI} a x^{bn_{qI}} e^{cn_{qI}x})^{2/3} \pi r_{c0}^2 & \text{for} \quad dpa < D_s \\ (C_{qII} a x^{bn_{qII}} e^{cn_{qII}x})^{2/3} \pi r_{c0}^2 & \text{for} \quad dpa \geq D_s \end{cases} \tag{4.8}$$

The radiation induced damage profile in the cylindrical portion of horn has been shown in Figure 4.6

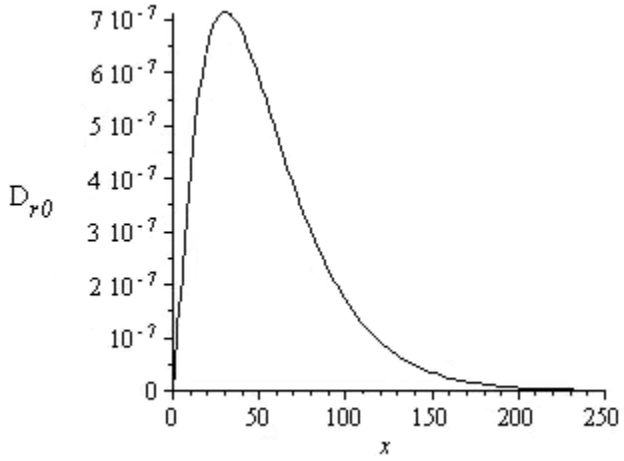

Figure 4.6: Radiation induced damage profile along the horn cylindrical tangent.

In order to compute the evolution of radiation induced micro-damage under the mechanical loads, the following evolution law (Riceand and Tracey 1969, Beremin 1981, Huang 1991, Pardoen et al. 1996) has been implemented:

$$dr_c = r_c \alpha_r exp\left(\frac{3\sigma_m}{2\sigma_{eq}}\right) dp \tag{4.9}$$

$$dD_{rm} = q_A dA_{rm} = q_A 2\pi r_{c0} dr_c \tag{4.10}$$

The current value of micro-damage for the i-th cycle is computed in additive way by means of the current value of radiation induced damage and its evolution under mechanical loads (compression-tension) expressed by the accumulated plastic strain p.

$$D^i_{rm} = D^i_{r0} + \int_0^p dD^i_{rm} \tag{4.11}$$

The evolution of micro-damage as a function of distance and number of cycles is shown in Figure 4.7.

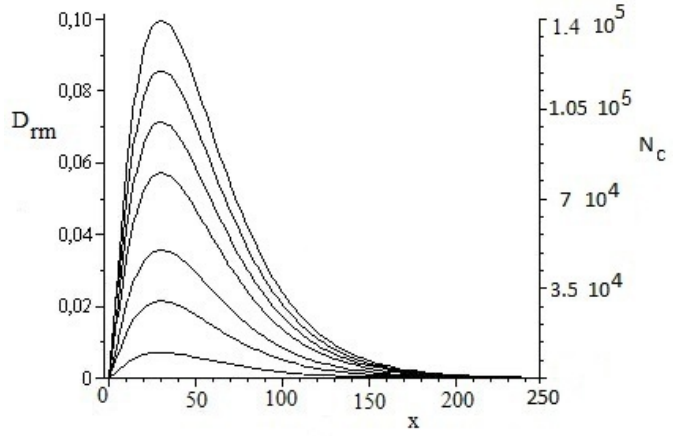

Figure 4.7: Evolution of micro-damage parameter as a function of distance and number of cycles.

The maximum micro-damage parameter is observed at a distance of 30-40 mm from the beginning of the cylindrical portion of the horn. The number of cycles to failure as a function of maximum dpa on single cycle is shown in Figure 4.8. It has been assumed that the failure occurs as soon as the maximum damage parameter, accumulated over all cycles, reaches the value of 0.1. Such a value is usually accepted as corresponding to the initiation of macro-crack.
Here, large sensitivity of the number of cycles to failure with respect to the maximum dpa induced on single cycle (beam deposition in the target, compression/traction) is well visible. On the other hand, the sensitivity of the number of cycles to failure with respect to the stress amplitude in the horn cylindrical portion (compression-tension) is practically negligible, as indicated in Figure 4.9.

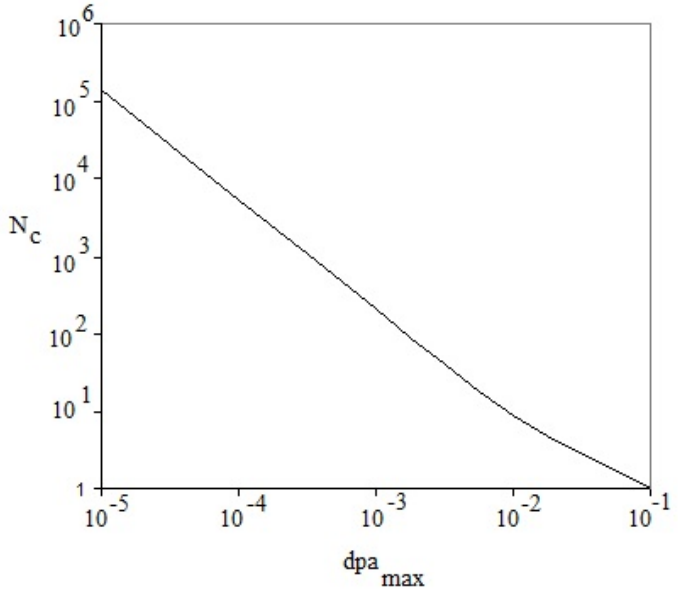

Figure 4.8: Number of cycles to failure as a function of maximum dpa on single cycle (log-log).

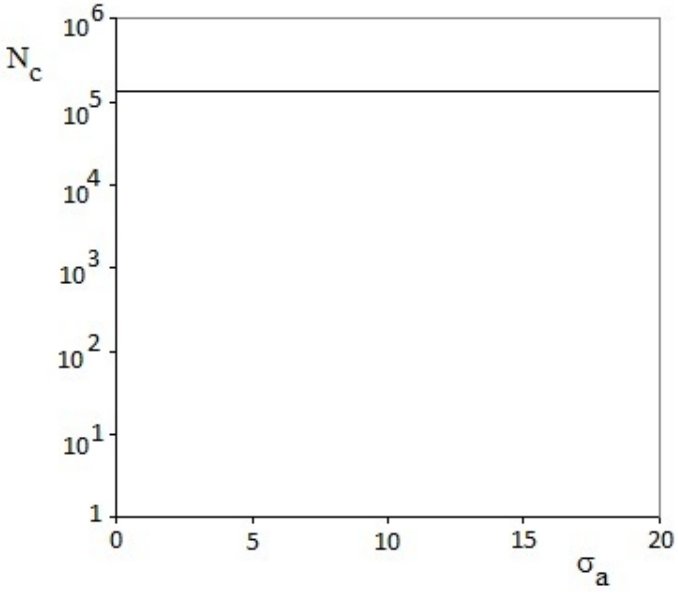

Figure 4.9: Number of cycles (log) as a function of the stress amplitude on cycle.

Conclusion:

It has been demonstrated in the course of the present study that the number of cycles to failure depends strongly on the accumulation of micro-damage due to irradiation, whereas the influence of the stress amplitude (within the range 0-20 MPa) on cycle is much smaller. For this reason it is fundamental to establish with a large certitude the maximum dpa on single cycle by means of numerical simulations and if possible by means of suitable experiment.

Chapter 5

Support system as a part of four horns integration

5.1 Introduction

The purpose of this part of the report is the assessment of various supporting system arrangements of the horns. This study begins with the static and dynamic analysis of a single horn support of a cantilever type, which is later introduced into a one frame support for two horns or four horns. In the second part the system of two frames is introduced for two or four horns arrangements, respectively. This study is also preceded by the analysis of a modified single horn support. The choice of respective thicknesses of the plates that form the supports, is made on the basis of parametric optimization results. The performed study concerns only the influence of the gravity forces and hydrostatic pressure of cooling water inside the horn shell on the stress distribution. No thermal effects (heat generation in the horn), no stress due to electrical current flow and no resulting magnetic stresses are taken into account at this stage of analysis.
The horn supporting systems which have been used so far in neutrino experiments like Miniboone, CNGS, T2K and so on are quite different. In the Miniboone experiment the horn shell was supported by a system of several vertical plates, which remained the classical saddle supports used in horizontal vessels. These plates where joined with relatively rigid housing (bottom frame). In the CNGS experiment the horn structure was joined with a rigid vertical frame on target introduction side. This frame was welded to the stiff bottom plate lying on rails. The truss for the cooling water supply was welded to the bottom

plate and joined in several areas to the horn shell also restraining it (see Figure 5.1). The relatively high stiffness of the supporting system restrained the total deflection of the structure with the whole attached to the horn shell equipment and kept the maximum value of stresses within the acceptable level.

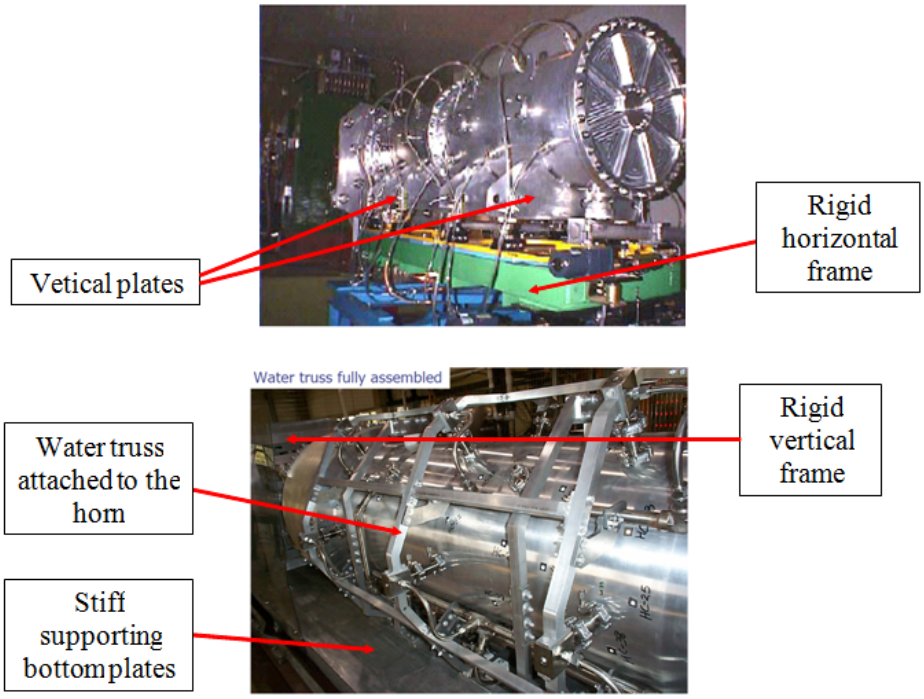

Figure 5.1: Miniboone and CNGS horn assemblies

In the case of a recent horn installation, namely T2K, the proposed support system is quite different - the horn is supported by the system of four pipes welded to a ring, which is welded directly on the horn shell. These pipes are placed in a certain axial distance on both opposite sides of the horn. The outer ends of the pipes are joined to the vertical rigid beams clamped on the top to a rigid frame. An additional support is provided by a set of alimentation plates (strip lines) attached at the same end where the target is introduced. The arrangement of supports proposed below makes use, to a certain extents, of the support concept proposed for CNGS experiment (support in vertical direction), and adopts concepts of vertical or horizontal assembly of the whole

horn structure.

5.2 Cantilever type support for a single horn.

The proposed design of the support system should satisfy several conditions. These are as follow. First of all, the structure should be rigid enough providing small displacements of horn under the system of loads considered. Second, due to omitting thermal, electrical and magnetic effects, which have an impulsive nature, the maximum equivalent stress in the horn structure should be kept at a level as low as possible, in order to keep the fatigue resistance of the horn as high as possible. Additionally, the assembled structure should exhibit relatively high frequencies of free vibrations in order to protect the structure of the horn and the support from possible resonance. As the basis for the analysis, the horn dimensions proposed by the CNRS Strasbourg were taken into account (see Figure 5.2). Also, the number, size and location of input holes for the water jet system and holes for the drain system were kept unchanged. It is assumed that the structure of the horn is made of aluminium alloy 6086 T6. For the support construction the same material is proposed. All numerical results presented below are valid in the absence of a water supply truss with a system of water supply pipes and drainage. Also, the influence of strip line plate attachments has not been analyzed yet.

The concept of the proposed support is illustrated in Figure 3. This proposal provides reasonable vertical stiffness of the support for a single horn and keeps its weight at an acceptable level. The dimensions of the main horizontal plate L_p, and B_p are assumed to be equal: $L_p = 2.2$ [m] and $B_p = 1.1$ [m] . The vertical position of the supporting plate was set to 0.85 m below the longitudinal axis of the horn, which provides enough room to introduce water truss and drainage system without the risk of collision. The width of the vertical plate was assumed to be the same as for the horizontal plate but its height was set to $H_z = 0.7$ [m]. These dimensions are shown in Figure 5.4. The shape of the vertical plates for the saddle supports shown in Figure 5.3 accounts for undercuts, which provide free run for the drain pipe placed below the horn shell. The shape and thickness of both saddle supports were assumed to be the same. The first support, placed at $z = 0.589$ [m], is joined with the supporting plate (fixed support) while the second, placed at $z = 1.696$ [m], serves as a sliding support. The vertical rib plates placed below the main horizontal plate increase the perpendicular stiffness of the support. Their height varies linearly from 0.60 m at the beginning to 0.05 m at the end, and is de-

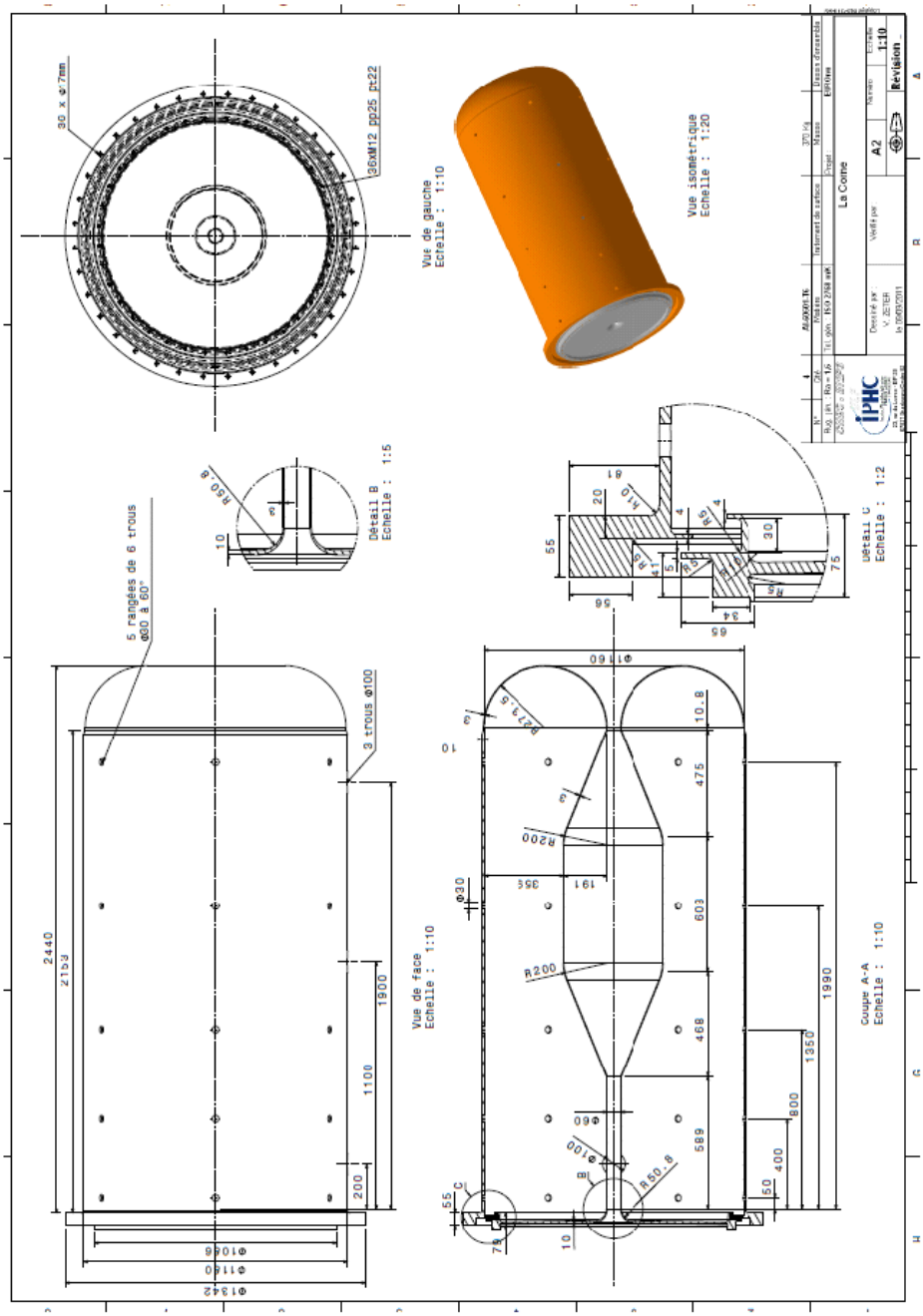

Figure 5.2: General view and dimensions of single horn (courtesy CNRS)

termined by the position of the gravity centre of the horn and the use of one frame only as a support for two horns. The choice of thickness for respective supporting plates was determined by several conditions. The first one was to keep the level of stress in the horn as low as possible, the second was the limit for the maximum vertical deflection, and this was assumed to stay below 0.5 mm in the vertical direction for horn without water truss frame and subjected only to gravity forces. Based on the above restrictions, a finite element model was prepared. The FEM package ANSYS [1] was used for detailed numerical calculations. Besides these limits resulting from static conditions, the limits on the natural frequencies were imposed - it was demanded to get their lowest values as high as possible. In the first step reasonable (from the engineering point of view) ranges of values for thickness of respective plates in support system were proposed. These values were as follow (see Table 5.1 and Figure 5.5 for thickness assignement):

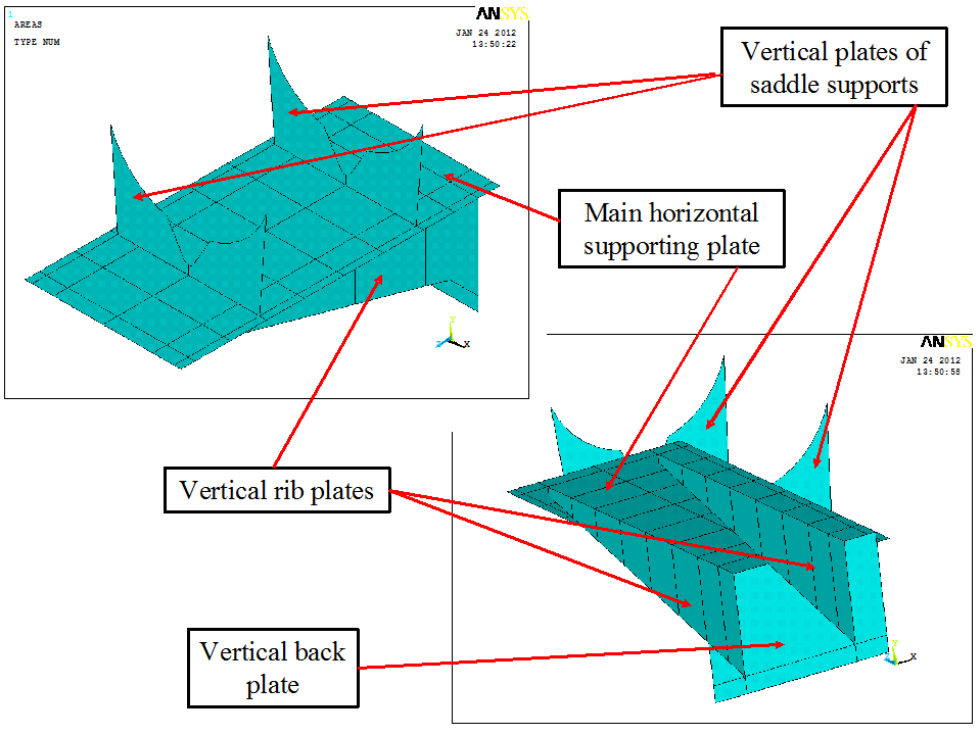

Figure 5.3: Proposed shape of support construction

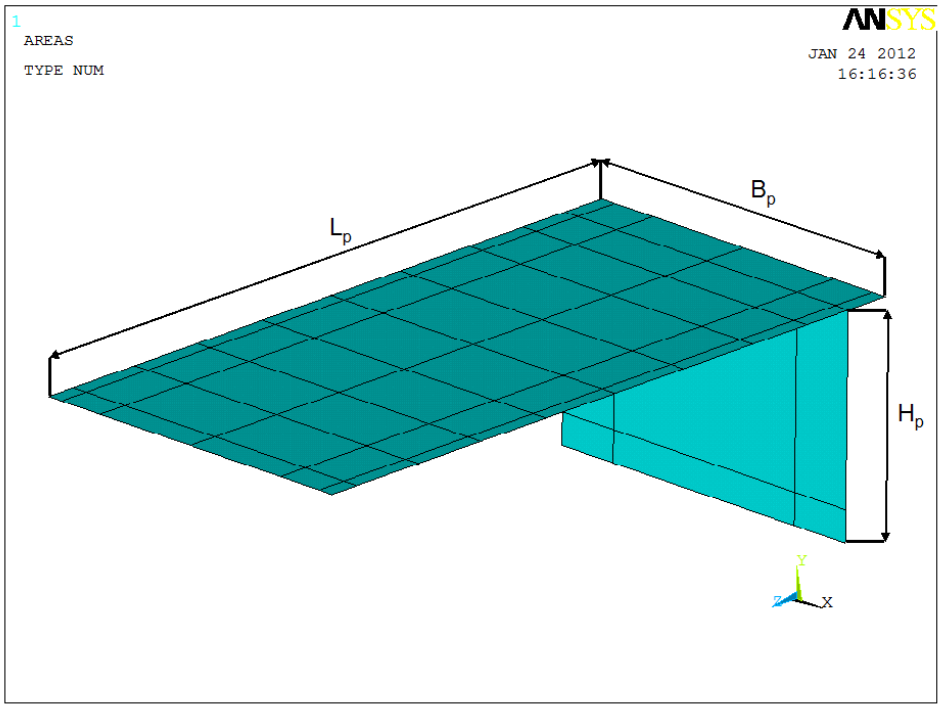

Figure 5.4: Main dimensions of main horizontal supporting plate and vertical back plates

Table 5.1: Admissible values of thicknesses for single horn support system

Thickness parameter description	Symbol	Minimum value in mm	Maximum value in mm
Horizontal supporting plate	t_{hp}	8.0	40.0
Vertical saddle support plate	t_{ss}	4.0	16.0
Vertical rib plates	t_{vr}	5.0	25.0
Vertical back plate	t_{bp}	8.0	25.0

In the analyzed numerical model the horn structure and the supporting plates were modeled with shell elements. The front plates of the horn have a more complex shape and in this case 3D solid finite elements were used. Both plates form a flange connection on their outer edge. To model this part

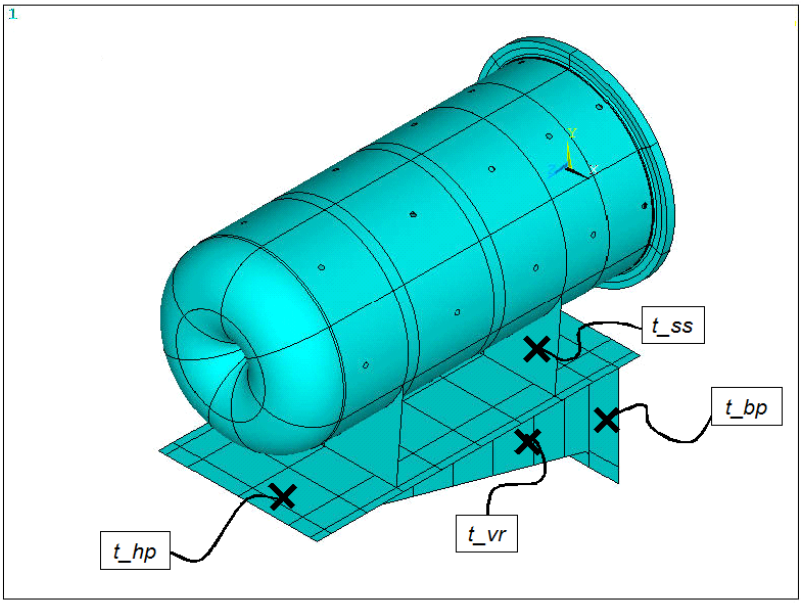

Figure 5.5: Single horn on a support with plate thickness assignement

one must use very dense and complex finite element mesh, which increases of the numerical effort. In order to alleviate this, the proposed model includes the coupling of displacements of selected nodes corresponding to the radial position of the connecting bolts. The support of the horn is arranged in the following way, both vertical plates working as saddle supports are welded to the outer skin of the horn shell. The first support (at $z = 0.589$ [m]) is a fixed support , while the second one (at $z = 1.696$ [m]) is a sliding one (the same vertical deflections u_y are considered along the bottom edge of the support). This arrangement admits axial and perpendicular (x direction) deflection of the horn caused by thermal expansion expected during operation. However, the temperature load is not considered at this stage of analysis. The whole structure is supported along two edges of the vertical back plate. The details of the model are presented in Figure 5.6, which shows the exemplary mesh of finite elements with all respective boundary and coupling conditions. The

mesh provides a reasonable compromise between the calculation time for a single run and the justified level of calculation error (not higher than 5% with respect to equivalent stress assessment).

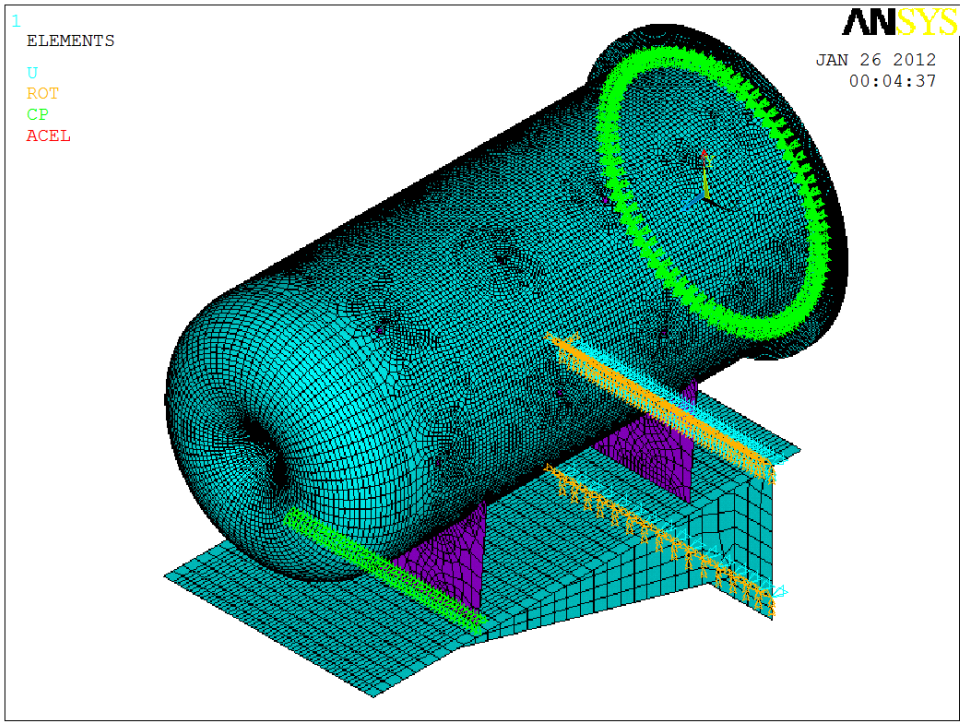

Figure 5.6: Finite element mesh of horn and support structure with boundary and coupling conditions

In the next step the structure subjected to its own weight was analyzed, the problem was the choice of optimal integer values for respective plate thickness. For this purpose, certain optimization process were performed. All plate thickness given in Table 5.1 cover certain ranges of values so that they were regarded as design variables. The optimization was done in two ways. In the first procedure the minimum weight of the whole support was searched with additional state conditions. These were as follow: the absolute value of maximum vertical deflection ($|u_y|$ displacement) should not exceed 0.5 [mm], the maximum equivalent stress in the horn structure itself was limited to $\sigma_{eqv}^{max} = 20$ [MPa], and the maximum stress in the support structure itself was set to $\sigma_{eqv}^{max} = 100$

[MPa]. In the second approach the minimum value of equivalent stress in the horn itself was set as an objective function. In this case the absolute value of the vertical deflection and maximum equivalent stress in supporting structure were introduced as state variables and their maximum values were assumed as previously. The results of the above described optimization are presented in Table 5.2

Table 5.2: Results of optimization process for static load

	Optimization 2	Optimization 1
Optimal values for design variables	$t_{ss} = 14.0$ [mm] $t_{ss} = 40.0$ [mm] $t_{ss} = 8.0$ [mm] $t_{ss} = 11.0$ [mm]	$t_{ss} = 4.0$ [mm] $t_{ss} = 10.0$ [mm] $t_{ss} = 5.0$ [mm] $t_{ss} = 10.0$ [mm]
Maximum absolute value for vertical deflection of horn $\|u_y\|_{max}$	0.41 [MPa]	0.32 [mm]
Maximum value of equivalent stress in horn σ_{eqv}^{max}	3.8 [MPa]	5.5 [MPa]
Maximum value of equivalent stress in support structure σ_{eqv}^{max}	15.6 [MPa]	15.3 [MPa]
Weight of the support structure M_{sup}	334 [kg]	113 [kg]

As can be seen, the maximum stress in the horn is low in both cases, also the maximum vertical deflection of the horn is within acceptable limits. The main difference cab be observed in the masses of the support systems, so that the combination of the thickness obtained in optimization 1 seems to be more interesting. In Figures 5.7 – 5.10 the main results of optimization 1 are presented, while Figures 5.11 – 5.14 illustrate results of optimization process 2. In these plots the shape of static deformation, vertical deflections in [m] and equivalent stress in [Pa] are presented. In both cases the maximum of the equivalent stress is observed in the vicinity of the vertical rib plate and vertical back plate bottom connection. This area is a stress concentration area, but the maximum value of stress does not differ in a mean sense and is fully acceptable.

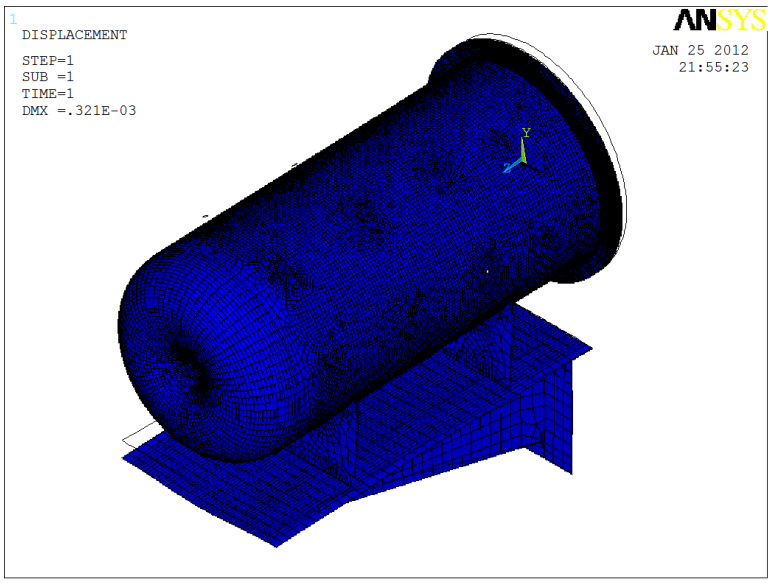

Figure 5.7: Optimization 1 – deformation of structure

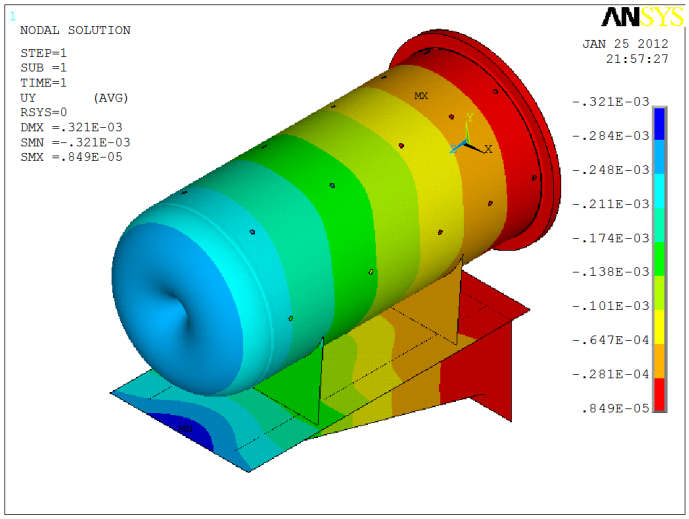

Figure 5.8: Optimization 1 – distribution of vertical displacements in [m] in horn and support structure

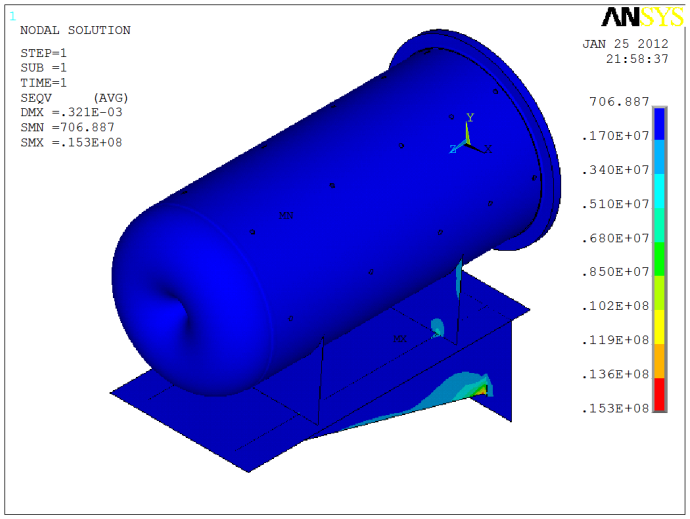

Figure 5.9: Optimization 1 – distribution of equivalent stress in [Pa] in horn and support structure

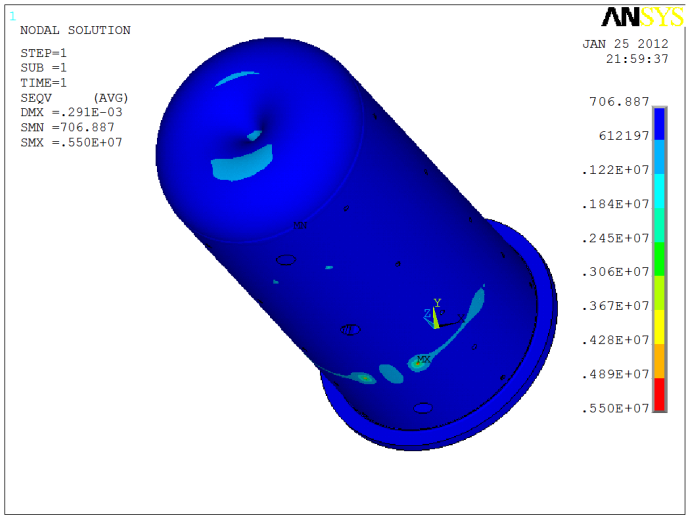

Figure 5.10: Optimization 1 – distribution of equivalent stress in [Pa] in horn

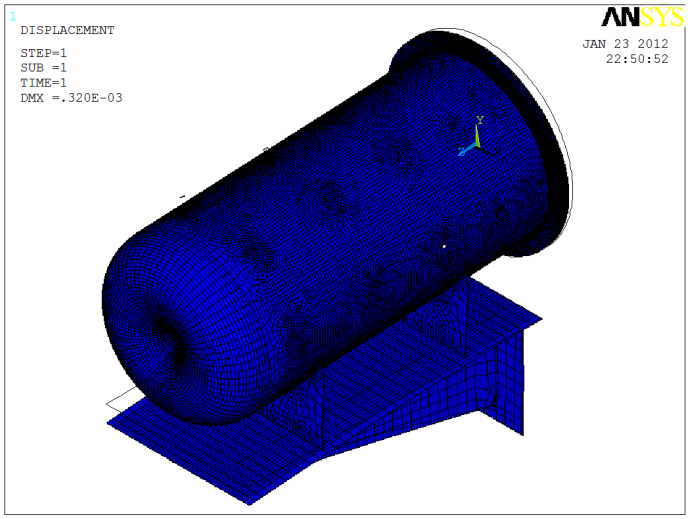

Figure 5.11: Optimization 2 – deformation of structure

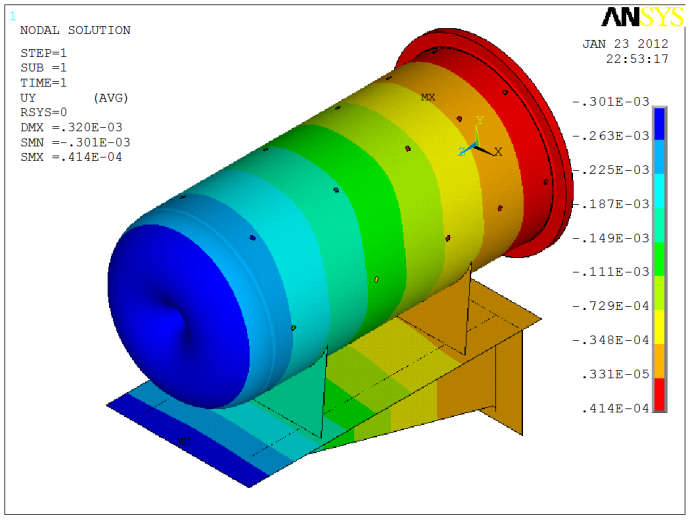

Figure 5.12: Optimization 2 – distribution of vertical displacements in [m] in horn and support structure

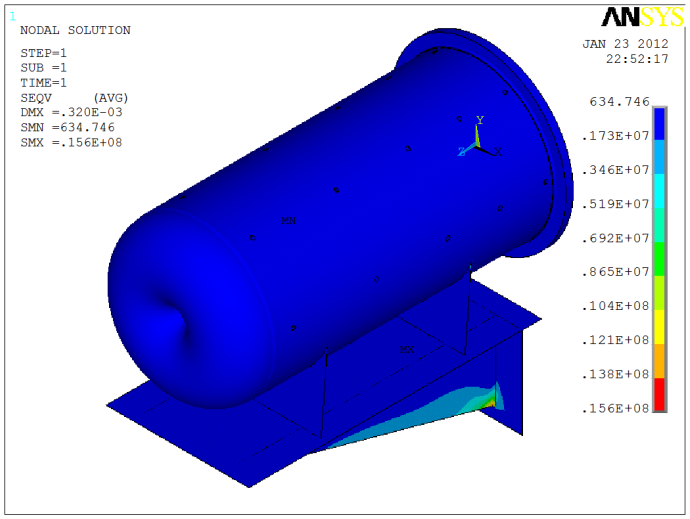

Figure 5.13: Optimization 2 – distribution of equivalent stress in [Pa] in horn and support structure

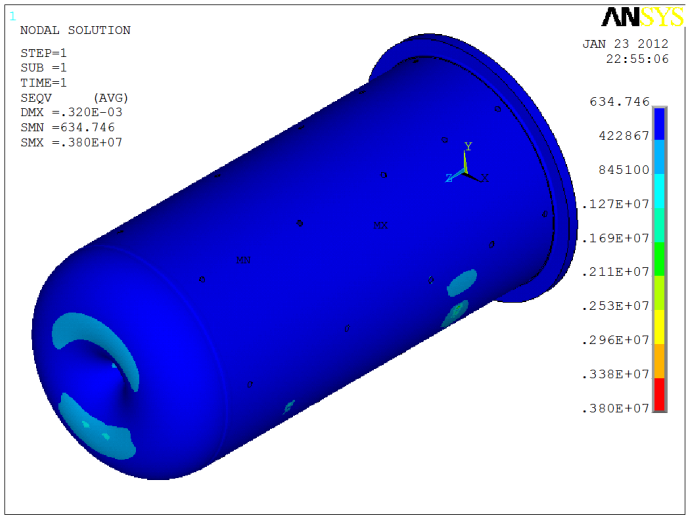

Figure 5.14: Optimization 2 – distribution of equivalent stress in [Pa] in horn

In the next step, the calculation of natural frequencies and mode shapes was performed for both optimized sets of thickness parameters. The summary of first twenty lowest natural frequencies is presented in Table 5.3 below.

Table 5.3: Lowest twenty natural frequencies in [Hz] for two optimal sets of parameters

Number of frequency	Optimization 1	Optimization 2
1	4.1271	5.9022
2	4.1646	13.411
3	27.609	34.964
4	29.374	44.190
5	32.555	49.040
6	33.056	50.157
7	35.177	64.436
8	40.161	74.757
9	47.884	86.319
10	48.768	87.328
11	54.748	87.468
12	56.326	91.605
13	62.289	92.603
14	64.626	116.14
15	65.602	118.54
16	69.779	125.85
17	82.107	132.60
18	84.637	140.84
19	87.261	143.13
20	87.691	151.15

As can be seen from these results, in the first column the structure is quite flexible from the dynamic point of view. The increase of thickness in all supporting plates – the set of values obtained in optimization 2 - results in a marked increase in the frequency values, however they are still not fully satisfying. The final assessment of the vibration levels needs to be done depending on the possible vibration sources (the dynamic load on the horn, excitation from the cooling system etc.). Figures 5.15 and 5.16 present the first four mode shapes for both sets of optimized parameters.

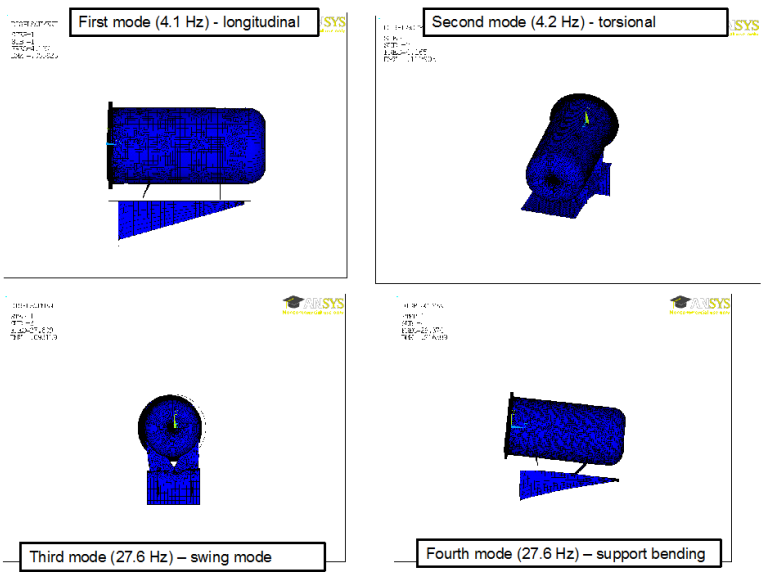

Figure 5.15: First four mode shapes for horn with optimization 1 parameters

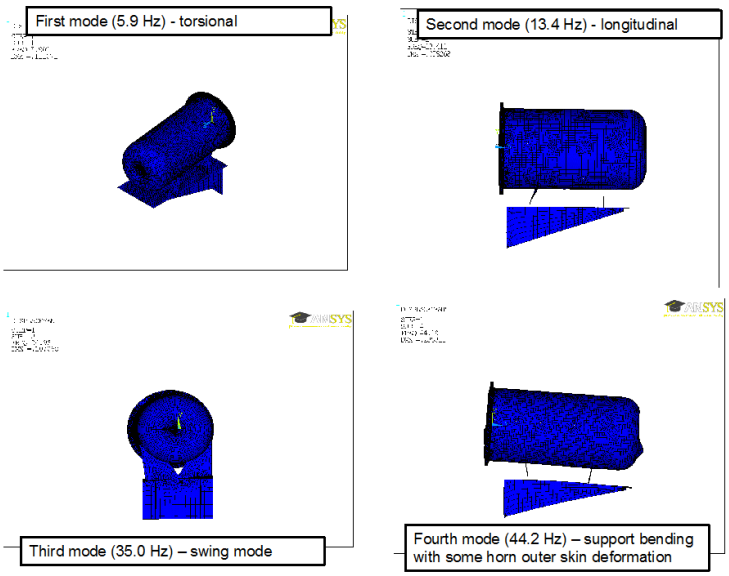

Figure 5.16: First four mode shapes for horn with optimization 2 parameters

Table 5.4: Influence of cooling water inside the horn on numerical results

	Optimization 2	Optimization 1
Optimal values for design variables	$t_{ss} = 14.0$ [mm] $t_{ss} = 40.0$ [mm] $t_{ss} = 8.0$ [mm] $t_{ss} = 11.0$ [mm]	$t_{ss} = 4.0$ [mm] $t_{ss} = 10.0$ [mm] $t_{ss} = 5.0$ [mm] $t_{ss} = 10.0$ [mm]
Maximum absolute value for vertical deflection of horn $\|u_y\|_{max}$ without cooling water inside	0.41 [MPa]	0.32 [mm]
Maximum absolute value for vertical deflection of horn $\|u_y\|_{max}$ with cooling water inside (Figure 5.18 and Figure 5.21)	0.44 [MPa]	0.56 [mm]
Maximum value of equivalent stress in horn σ_{eqv}^{max} without cooling water inside	3.8 [MPa]	5.5 [MPa]
Maximum value of equivalent stress in horn σ_{eqv}^{max} with cooling water inside (Figure 5.19 and Figure 5.22)	8.2 [MPa]	11.0 [MPa]

The horn structure is subjected to a complex system of loadings. One of the main results is the temperature increase in the whole structure and in the horn inner part close to the target space. In order to keep the temperature increase within the acceptable range a system of water jets is installed on the outside skin of the horn. To provide a continuous flow and removal of the cooling water a system of drains is installed at the bottom part of the horn exist. However, some volume of water may still remain inside the horn. Further numerical calculations try to assess the influence of the water in horn on the deflections and equivalent stress values and distributions. Two optimized sets of parameters for the supporting plates were analyzed and it was assumed that the free surface of the cooling water rises at most to the edges of water jet holes located at the minimum vertical position of the horn. On this basis the respective hydrostatic pressure was calculated and applied in the lower part of the horn. A summary of the results is given in Table 5.4. Figure 5.17 shows the distribution of hydrostatic pressure resulting from water imposed on the inside face of the horn outer shell while Figures 5.18 to 5.22 give the distributions of vertical deflections and equivalent stress for both the discussed cases.

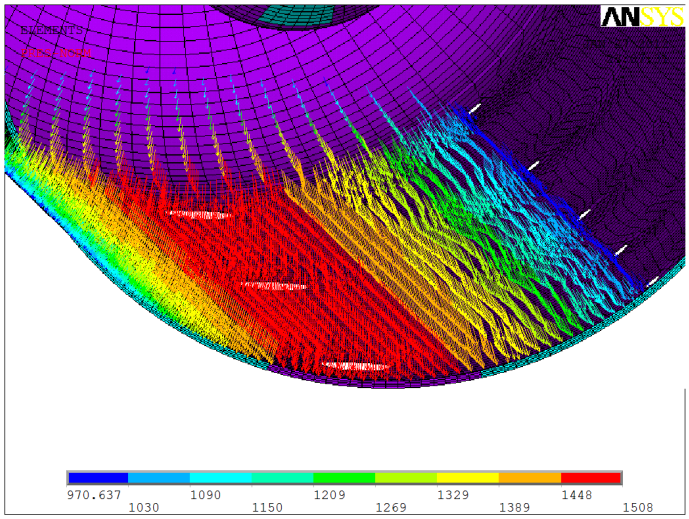

Figure 5.17: Cooling water inside horn - hydrostatic pressure distribution, pressure in [Pa]

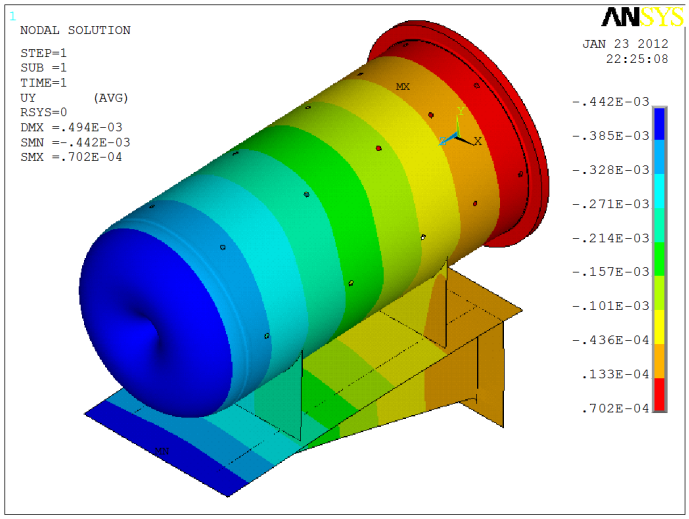

Figure 5.18: Distribution of vertical deflections for horn with cooling water inside, optimization set 2

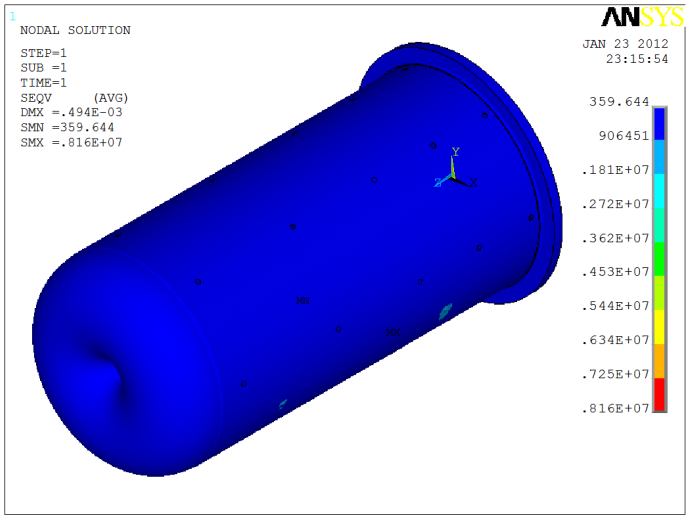

Figure 5.19: Distribution of equivalent stress in horn for structure with cooling water inside, optimization set 2

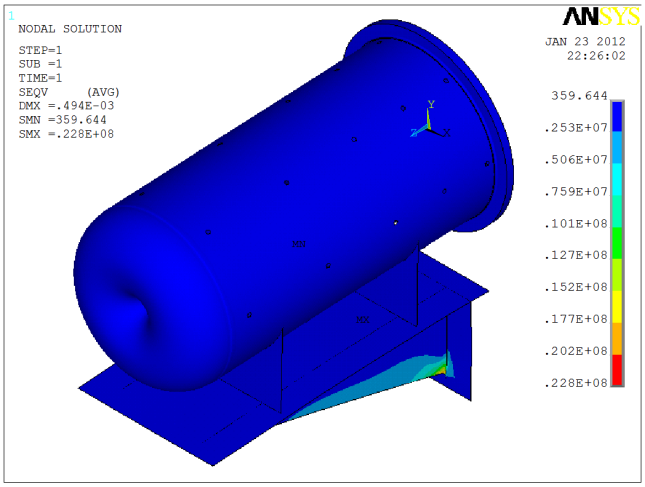

Figure 5.20: Distribution of equivalent stress for horn and supporting structure with cooling water inside, optimization set 2

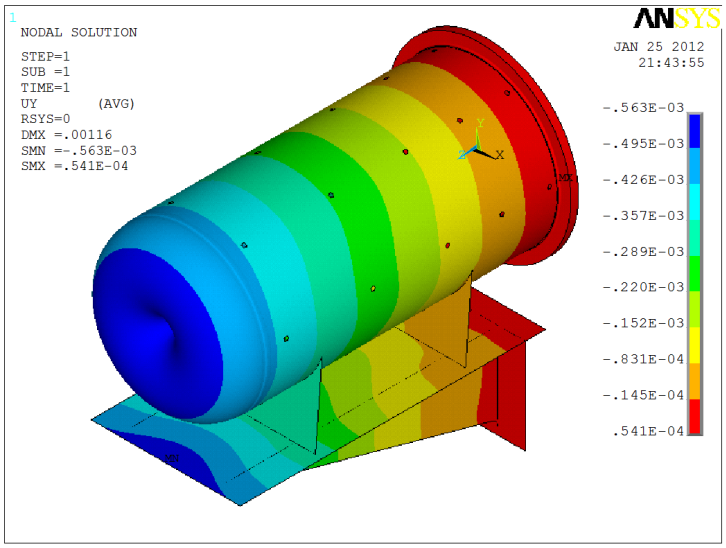

Figure 5.21: Distribution of vertical deflections for horn with cooling water inside, optimization set 1

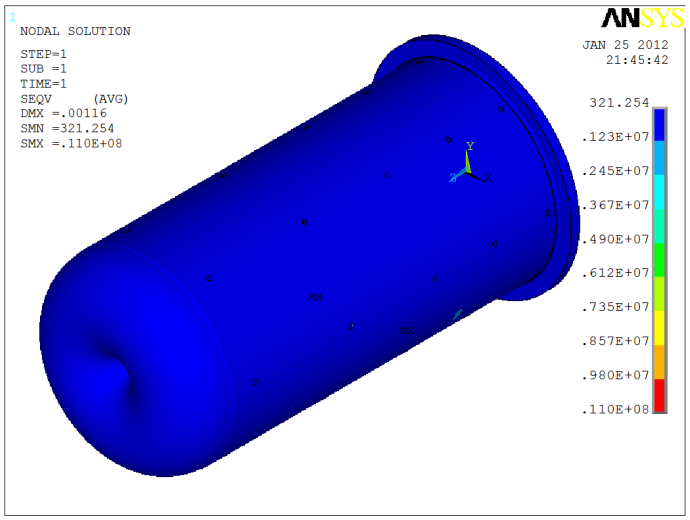

Figure 5.22: Distribution of vertical deflections for horn with cooling water inside, optimization set 1

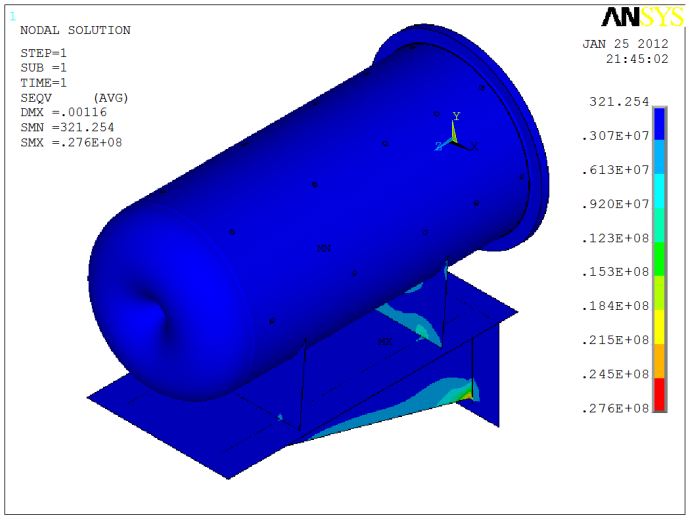

Figure 5.23: Distribution of equivalent stress for horn and supporting structure with cooling water inside, optimization set 1

The comparison of the results shows better performance (higher stiffness) of supporting plate parameters obtained in optimization 2, this observation is of a similar nature as the results of the dynamic analysis. Due to this, it has been decided that further analysis of two horns assembled in a single frame will be performed using the parameters obtained in optimization run 2.

5.3 Supporting frame concepts

The assembly of four horns, the introductory concept of which is shown in Figure 5.24, should provide easy operation and adjustment of the whole system, as well as high stiffness of the supporting system and as high as possible values of the natural frequencies of the whole structure. Additionally, the size of the cavern for four integrated horns is limited and influences the horn arrangement. In general, the height (maximum 4600 [mm]) and width (maximum 5300 [mm]) presented in Figure 5.24 below should not be exceeded. It is not definitely stated at the moment whether four horns should be arranged in one support system, or two supports for every two vertically placed horns are admitted. Therefore, numerical studies predicting both scenarios are presented in this report. First of all, results for a single one-side frame for two horns is presented.

This arrangement provides independent assembly for every two horn and is suitable for both horizontal insertion of horns into the frame system and can also be used in the case of vertical insertion by means of a crane system. The proposed supporting frame is made as a welded one and the basic cross-section makes use of the typical commercial channel sections, here the authors studied the properties of channel section with dimensions as follows: $b \times s \times t = 160 \times 60 \times 15$ (all dimensions in mm). The details are shown in the Figure 5.25. In the next plot, Figure 5.26, the front view of the basic cell for one horn with a cooling water truss is shown. It is assumed that the clearance between the outer skin of the water truss and the frame wall is not less than 30 [mm] in the vertical direction (top of horn) and 50 [mm] in the horizontal direction. As a result, the span of the frame was set to 1860 [mm] in the horizontal direction, while it is 1680 [mm] in the vertical direction. The provisional arrangement of two vertically placed horns is shown in Figure 5.27. This provides enough space for vertical back plate installation (Figure 5.5, design parameter t_{bp}) and as a consequence two horns were placed with a minimum vertical distance $l = 2547.5$ [mm].

5.4 Two horns assembled in a one-side frame support

The proposed support system must provide relatively easy horn position adjustment, which could compensate for the deflection of the frame and the horn itself and keep proper alignment with the particles produced in the target. The vertical positioning of the support system is easy to obtain even by means of a system of vertically mounted bolts attached to the top edge of the frame. On the other hand the tilt of the horn can be compensated for by means of two adjusting screws for each horn joining the lower part of each vertical back plate with neighboring horizontal beam of the truss. An introductory concept of this proposal is marked on the left side of the plot shown in Figure 5.29. However, the influence of the tilt on stress and deflection distributions has not yet been studied. The numerical study was performed for the set of boundary conditions as follow: the top edge of the frame was clamped while the bottom ends of vertical beams had blocked their deflections in the 'z' direction and rotations also around 'z' axis (see Figure 5.30). This situation corresponds to the vertical insertion of the support frame. The respective calculations of the support system with bottom edges clamped, which refers to the horizontal insertion of the horns were also performed. However, the latter resulted in much higher values of displacements and stresses, and these results are not included

Figure 5.24: Introductory concept of four horn arrangement (coutresy CNRS)

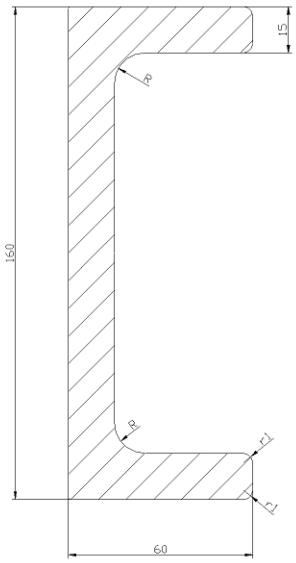

Figure 5.25: Dimensions of cross-section of channel segment used for supporting frame

in the report.

Figure 5.31 presents the total deformation of the support system. As can be seen the maximum deformation reaches 5 [mm], approximately. Figures 5.32 and 5.33 show the vertical ('y' axis) and horizontal ('z' axis) deflections, respectively. The results are given in [m]. The maximum absolute value of the vertical displacement is 4.2 [mm] and it occurs on the top of the outer skin of bottom horn. The maximum absolute value of the axial displacements ranges to 3.5 [mm] and takes place in the middle of the supporting frame. Figure 5.34 shows the distribution of the equivalent stress. The results for the stress are given in [Pa], and one can see that the maximum equivalent stress reaches 41 [MPa], which is acceptable. In Figure 5.35 the distribution of equivalent stress in the horns is shown, the maximum stress in this part of structure goes to 29 [MPa], which seems to be fully acceptable at this stage of analysis. The next plot presents the distribution of the equivalent stress in the frame system. Here, the maximum equal to 41 [MPa] and is reached in the connection of the supporting vertical back plate attached to the horizontal section of the frame

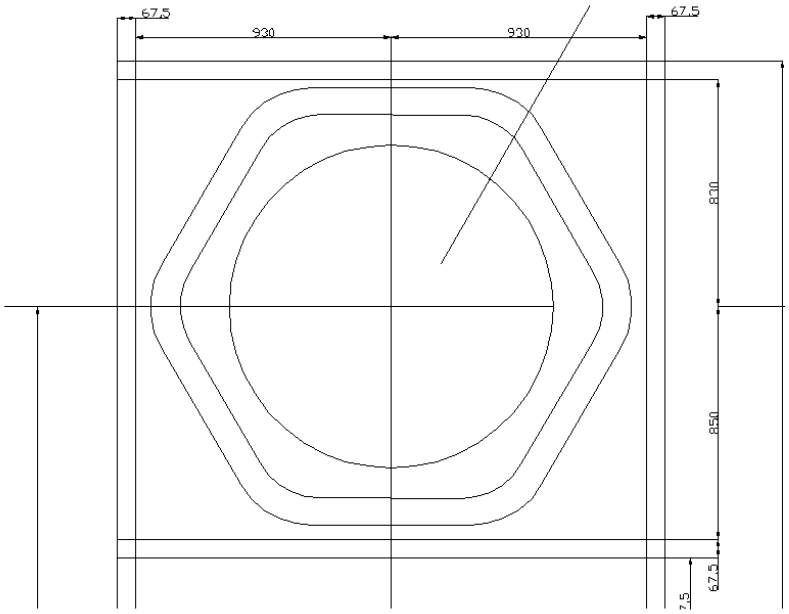

Figure 5.26: Basic cell for one horn with cooling water truss around horn - dimensions of basic cell

just below the top horn position. Although the results are acceptable from the strength point of view, an alternative support system is also being studied now.

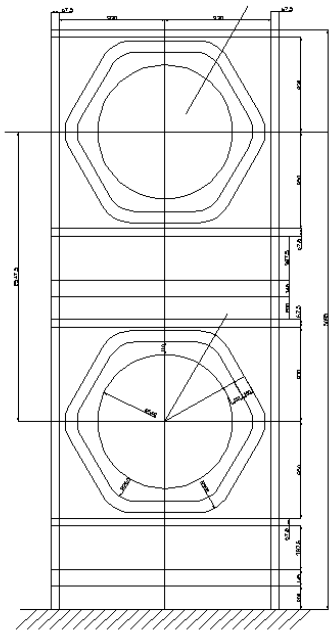

Figure 5.27: Front view of vertical arrangement of two horns

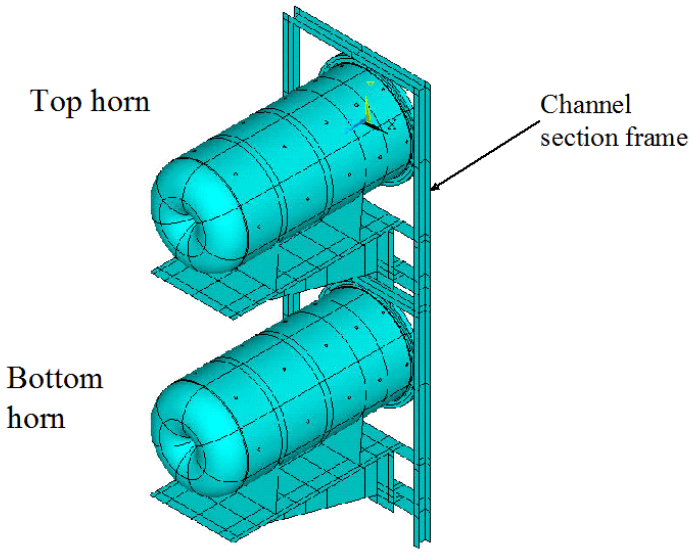

Figure 5.28: Isometric view of support system for two vertically placed horns

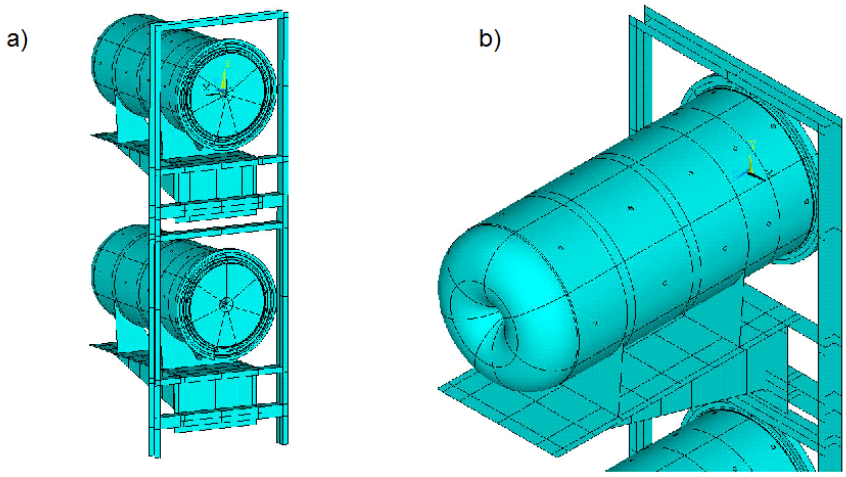

Figure 5.29: Adjusting screws concept for tilt compensation

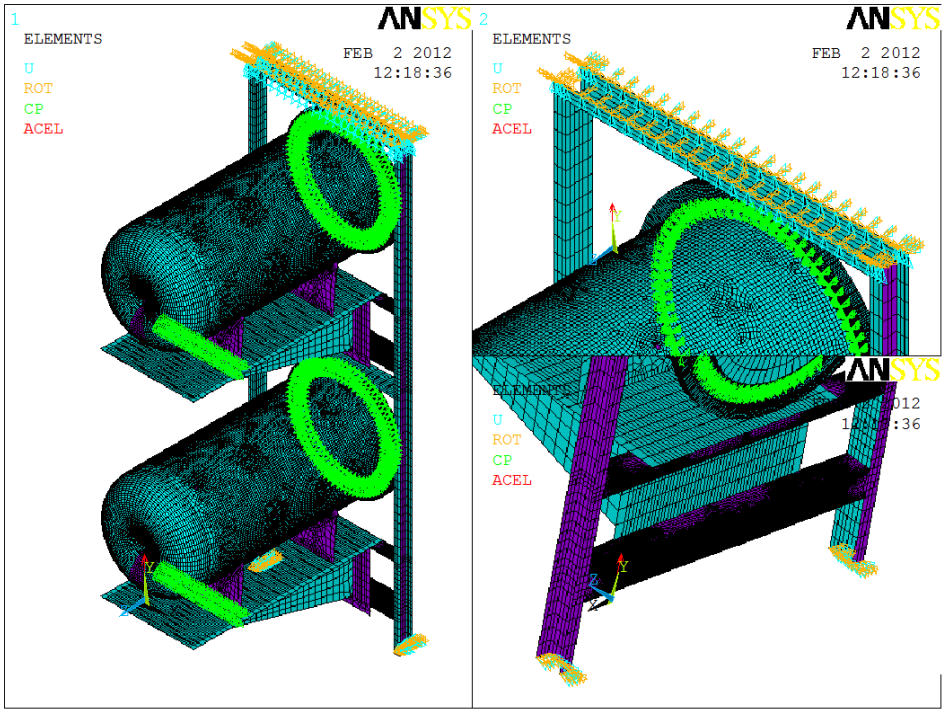

Figure 5.30: Mesh and boundary conditions for proposed support system

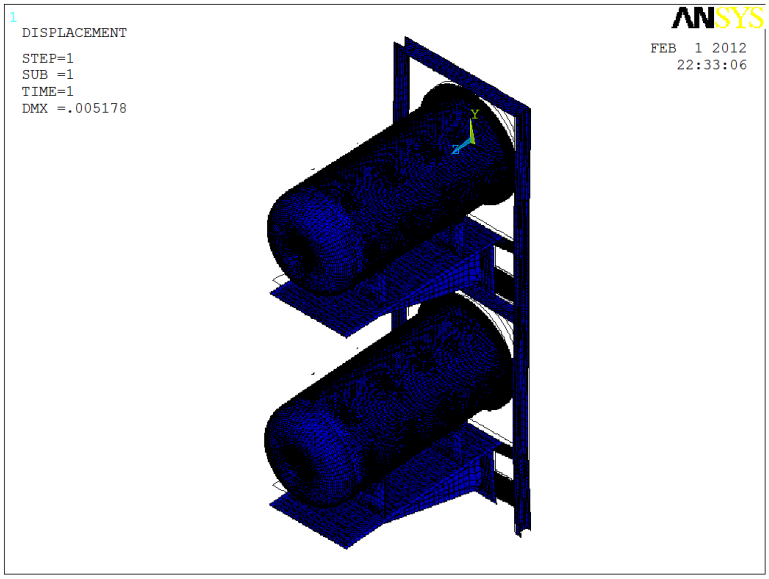

Figure 5.31: Deflection of support system for two horns

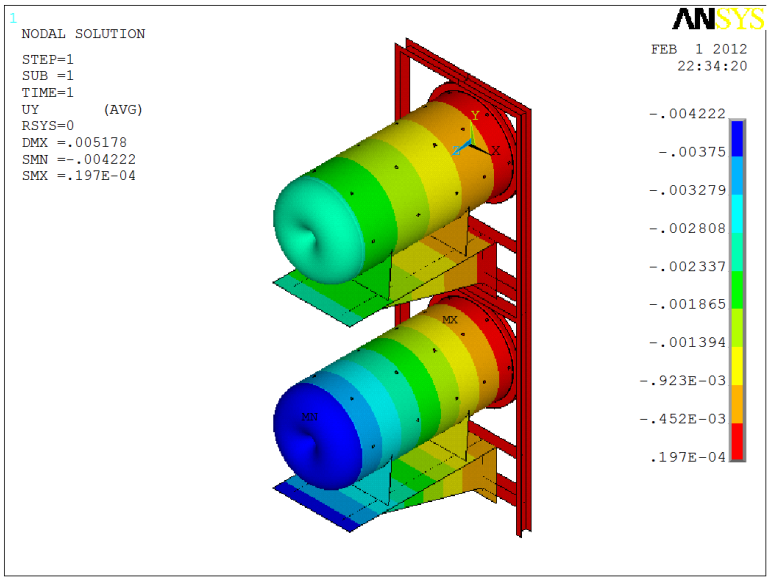

Figure 5.32: Vertical deflections of two frame support system in [m]

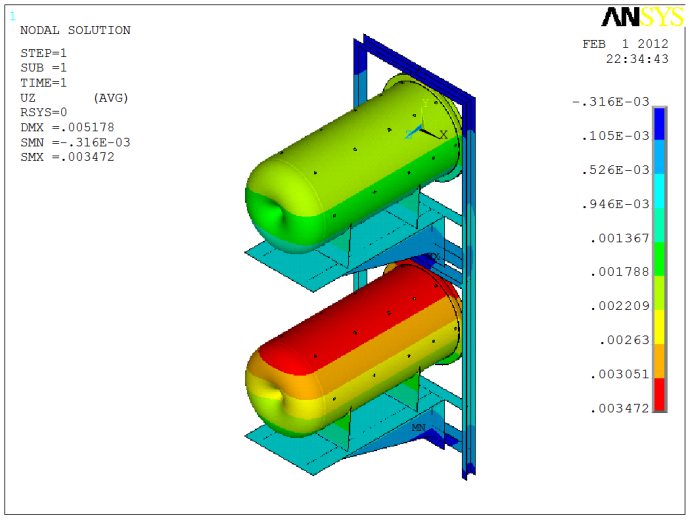

Figure 5.33: Deflections along 'z' axis of two frame support system in [m]

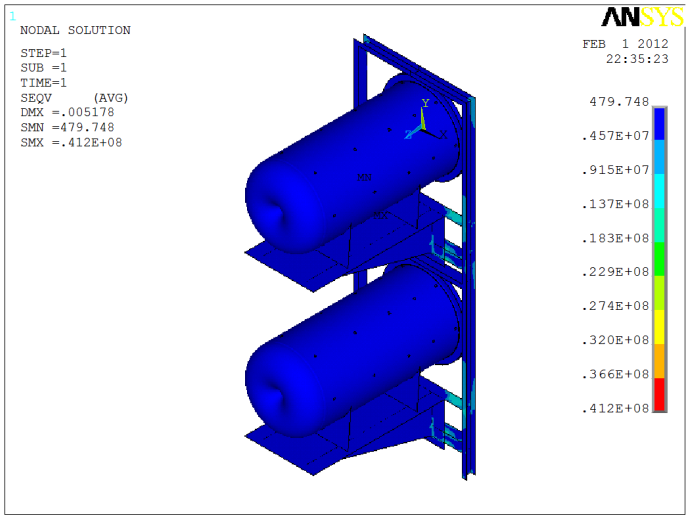

Figure 5.34: Distribution of equivalent stress in two horns arrangement in [Pa]

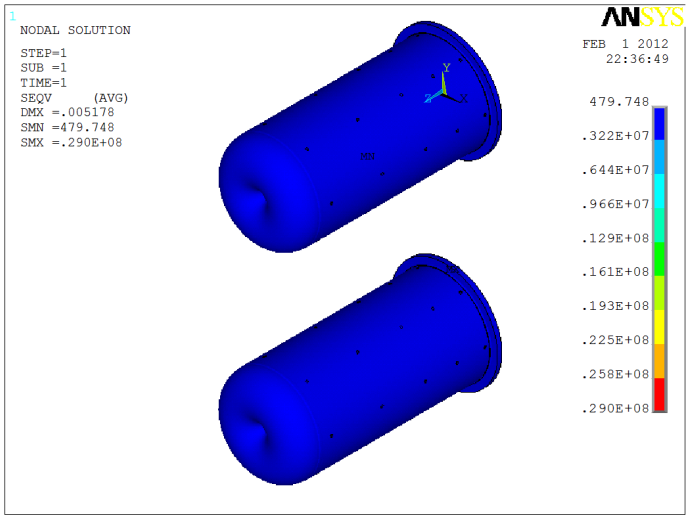

Figure 5.35: Distribution of equivalent stress in horns in [Pa]

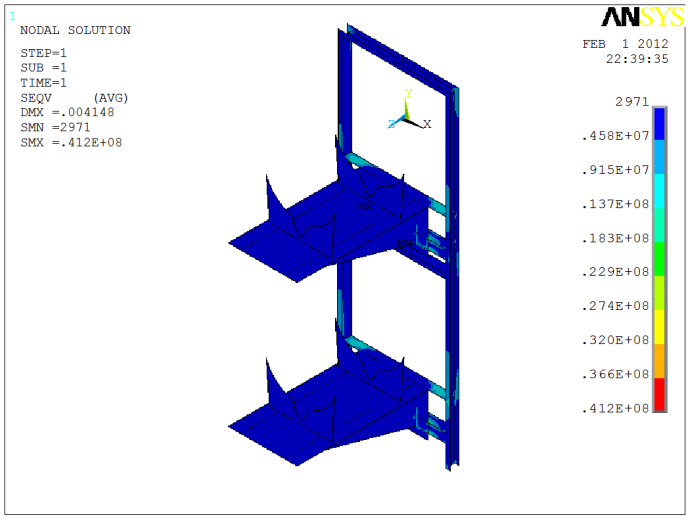

Figure 5.36: Distribution of equivalent stress in supporting frame in [Pa]

Chapter 6

A concept of solid target-horn integration

In the course of target-horn integration studies the following assumptions have been made (cf. EUROnu WP2 Note 11-01):

- Target station composed of 4 targets and collectors is envisaged
- The consecutive beam pulses will be sequentially directed to one of the four targets/collectors
- Each of four targets will be embedded in the bore of the relevant conventional pulsed current magnetic horn (inside magnetic reflector)
- Within 4-target assembly, each target is designed for 1 MW beam
- For the sake of simplicity, a solid beryllium target has been analysed as an option

The position of target in the bore of magnetic horn is shown in Fig. 6.1. The target-horn assembly is expected to withstand the beam induced heating, the primary and the secondary static and dynamic stresses as well as high level radiation (primary and secondary particle fluxes). As a significant heat load is deposited by the beam inside the target (high heat generation rate), an efficient cooling system is required. Moreover, the target is expected to withstand thermo-mechanical stresses arising from the impact load generated by the beam as well as from beam induced heating. In addition, degradation of material properties due to the evolution of radiation induced damage should be

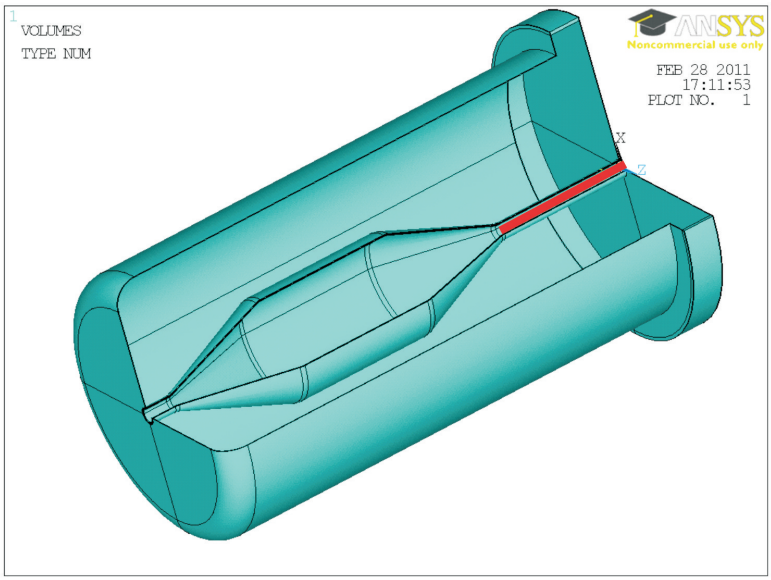

Figure 6.1: Layout of Superbeam target and the horn

accommodated. Similar requirements were defined w.r.t. the horn bore, that is understood here as the cylindrical thin-walled shell surrounding the pencil-like target. This part of the horn is subjected to Joule heating, quasistatic and dynamic stresses generated by heating/cooling cycles and pulse excitations as well as secondary particle flux coming from the target. The incident particles cause evolution of micro-damage that remains the origin of possible horn failure. Therefore, correct target-horn integration is fundamental for the reliability of the set-up. A concept of solid target-horn integration is shown in Fig. 6.5. Even if this proposal does not constitute the baseline, it allows to better understand the configuration of pencil-like target coaxially located in the inner conductor. In the presented concept, the target constitutes separate component w.r.t. the magnetic horn and has its own cooling system based on the flow of helium. The advantage of the solution consists in the fact that the target is cooled by the mass flow of helium, independently from the horn cooling system based on water sprays. Another advantage consists in the fact, that in this solution the target can be easily removed and replaced remotely. The concept of target embedded in the horn bore has been modelled by means of the FE method (Fig. 6.2). Thermal link between the target and the horn

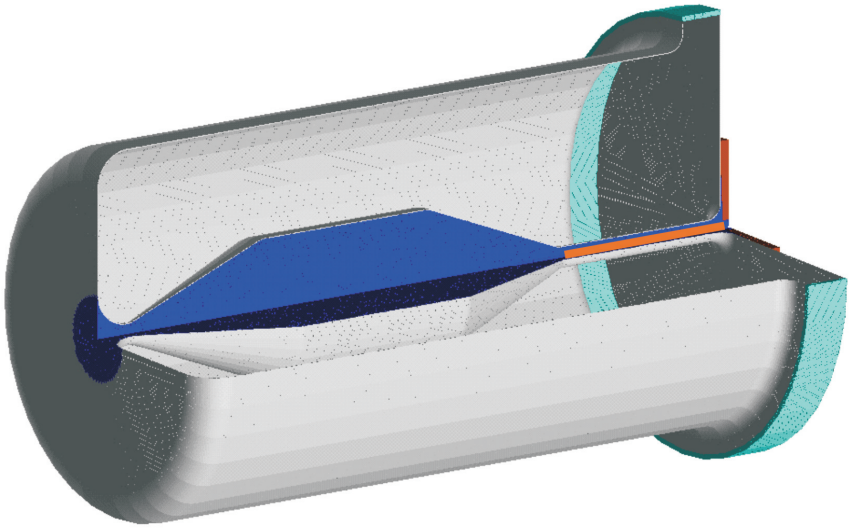

Figure 6.2: Target embedded in the horn bore (FE model)

wall based on the radiation has been assumed.

The temperature distribution in the horn wall, corresponding to the interaction between target and horn (heating and cooling sources taken into account), is shown in Fig. 6.3.

Similarly, the stress distribution in the horn wall corresponding to the target-horn interaction is shown in Fig. 6.4. The highest temperature is observed in the horn bore, in direct proximity of the target. The maximum temperature reaches some 337.5 K. On the other hand, the maximum equivalent stress is found in the outer part of the end plate and reaches some 12.5 MPa. Slightly enhanced stress state is observed in the opposite extremity of the horn bore w.r.t. the end plate. Generally, both the temperature and the stress levels in the horn inner conductor, computed in direct proximity of the target,

are acceptable from the point of view of the horn design. The above studies have shown that the following postulates related to target-horn integration are satisfied:

- Removing the beam heating of the target and the Joule heating of the horn are feasible
- Separation of the target from the horn increases modularity (assembly, maintenance, replacement) and permits efficient cooling solutions for both of them
- The thermal stresses in the horn inner conductor are fully acceptable, also for the Joule heating induced by the horn current pulses (efficient cooling)
- It is possible to adjust the target and the horn geometry separately, including the radial and the longitudinal alignment of both of them
- Failure modes of the target and the horn result mainly from irradiation (dpa) and thermo-mechanical cyclic loads and are only partially coupled
- Target can be easily removed and reinstalled inside the horn bore, thus reducing the cost of repair and the quantity of radioactive waste

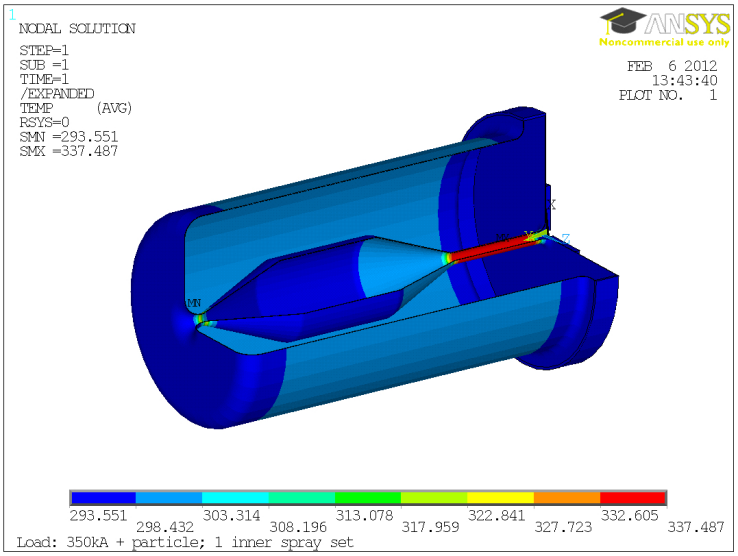

Figure 6.3: Temperature distribution in the horn wall corresponding to target-horn interaction

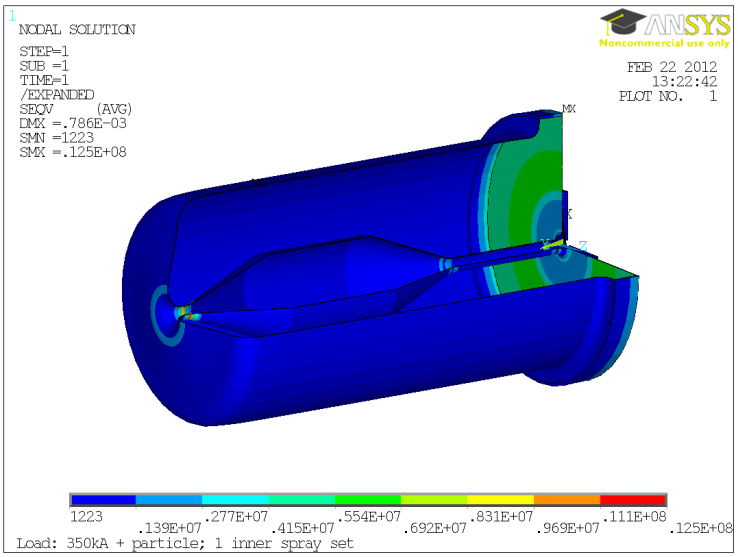

Figure 6.4: Stress distribution in the horn wall corresponding to target-horn interaction

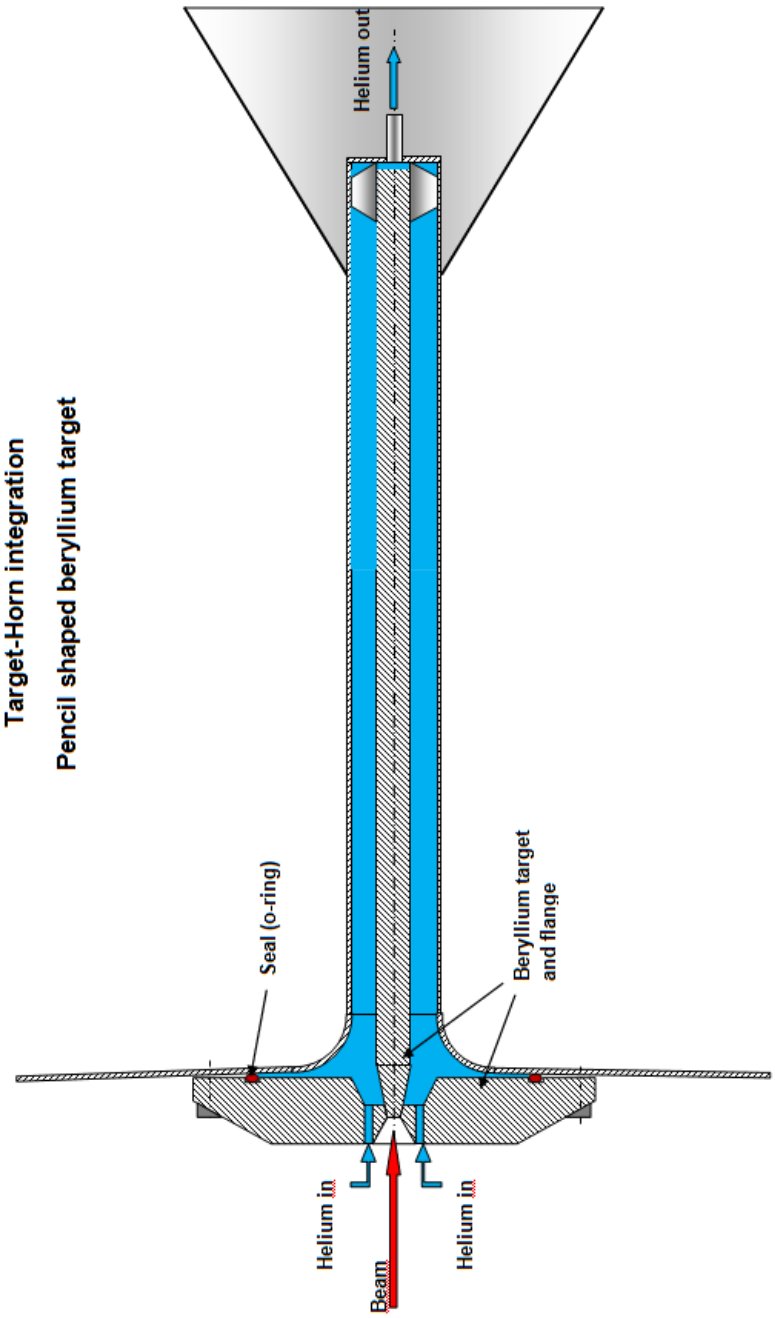

Figure 6.5: Pencil-like target integrated in the cylindrical part of the horn inner conductor

References

[1] *The Aluminium Federation web site (www.alfed.org.uk).*

[2] *Corrosion.* Newnes-Butterworths, London, 1976.

[3] *EUROCODE 9,Design of aluminum structures, Part 1.1 Structural design*, 1998.

[4] C. Bobeth et al. The target and horn for the SPL-based Super Beam: preliminary design report". EuroNu WP2 Note 11-01, February 2011.

[5] H.E. Boyer. *Atlas of Fatigue Curves.* American Society for Metals, Metals Park, Ohio, 1986.

[6] P. Cupiał. Miniboone-like horn: dynamic response to magnetic and thermal pulses. In *EUROnu Annual Meeting*, Rutherford Appleton Laboratory, January 2011.

[7] C.J. Densham. Conceptual design study of the long baseline neutrino experiment (LBNE) target and beam window. Technical report, STFC Rutherford Appleton Laboratory, November 2010.

[8] N.E. Dowling. *Mechanical Behaviour of Materials. Engineering Methods for Deformations, Fracture and Fatigue.* Prentice-Hall International Editors Inc, Englewood Cliffs, 1993.

[9] S. Kocanda and J. Szala. *Bassis of fatigue computations (in Polish).* PWN, Warszawa, 1999.

[10] M.S. Kozień and B. Szybiński. Method of time-life estimation of vibrating engineering structures with irregular time history response. In *Abstracts of the 5th International Conference on Very High Cycle Fatigue*, Berlin, 2011.

[11] M.S. Kozień, R. Valbuena, and P. Cupiał. Dynamic and fatigue analysis of the gran sasso horn. Technical note, CERN.

[12] P. Lutkiewicz. *The tightness conditions of UHV all-metal seals subjected to the radiation and inelastic deformation.* PhD thesis, Cracow, 2009. Supervisor B. Skoczeń.

[13] P. Lutkiewicz and B. Skoczeń. Evolution of irradiation induced micro-damage fields in ductile materials subjected to plastic deformation. In publication process.

[14] The Materials Information Society, ASM International. *ASM Handbook. Vol.19: Fatigue and Fracture*, 1996.

[15] J.-M. Maugain, S. Rangod, and F. Voelker. Study of a horn with integrated target for a neutrino factory. Nufact note 80, CERN, May 21st, 2001.

[16] A. Niesłony and E. Macha. *Spectral Method in Multiaxial Random Fatigue.* Springer, Berlin-Heidelberg, 2007.

[17] B. Skoczeń. Evolution of irradiation micro-damage. 2011. Presentation at CERN.

[18] P. Wertelaers. Magnetic pressure and mechanical considerations on a new design for the gran sasso neutrino beam. Ep 99-135, CERN, 30 August 1999.